Underlying event properties in pp collisions at root s=13 TeV

Alice Collaboration

Published in:
Journal of High Energy Physics (Online)

DOI:
10.1007/JHEP04(2020)192

Publication date:
2020

Document version
Publisher's PDF, also known as Version of record

Published for SISSA by Springer

Received: November 17, 2019
Accepted: March 24, 2020
Published: April 29, 2020

Underlying event properties in pp collisions at $\sqrt{s} = 13$ TeV

The ALICE collaboration

E-mail: ALICE-publications@cern.ch

Abstract: This article reports measurements characterizing the Underlying Event (UE) associated with hard scatterings at midrapidity ($|\eta| < 0.8$) in pp collisions at $\sqrt{s} = 13$ TeV. The hard scatterings are identified by the leading particle, the charged particle with the highest transverse momentum ($p_{\mathrm{T}}^{\mathrm{leading}}$) in the event. Charged-particle number-densities and summed transverse-momentum densities are measured in different azimuthal regions defined with respect to the leading particle direction: Toward, Transverse, and Away. The Toward and Away regions contain the fragmentation products of the hard scatterings in addition to the UE contribution, whereas particles in the Transverse region are expected to originate predominantly from the UE. The study is performed as a function of $p_{\mathrm{T}}^{\mathrm{leading}}$ with three different p_{T} thresholds for the associated particles, $p_{\mathrm{T}}^{\mathrm{track}} > 0.15$, 0.5, and 1.0 GeV/$c$. The charged-particle density in the Transverse region rises steeply for low values of $p_{\mathrm{T}}^{\mathrm{leading}}$ and reaches a plateau. The results confirm the trend that the charged-particle density in the Transverse region shows a stronger increase with $\sqrt{s}$ than the inclusive charged-particle density at midrapidity. The UE activity is increased by approximately 20% when going from 7 TeV to 13 TeV pp collisions. The plateau in the Transverse region ($5 < p_{\mathrm{T}}^{\mathrm{leading}} < 40$ GeV/c) is further characterized by the probability distribution of its charged-particle multiplicity normalized to its average value (relative transverse activity, R_{T}) and the mean transverse momentum as a function of R_{T}. Experimental results are compared to model calculations using PYTHIA 8 and EPOS LHC. The overall agreement between models and data is within 30%. These measurements provide new insights on the interplay between hard scatterings and the associated UE in pp collisions.

Keywords: Hadron-Hadron scattering (experiments)

ArXiv ePrint: 1910.14400

https://doi.org/10.1007/JHEP04(2020)192

Contents

JHEP04(2020)192

1 Introduction

In proton-proton (pp) collisions, particles originating from partonic scatterings with large 4-momentum transfer Q compared to the Quantum Chromodynamics (QCD) scale Λ_{QCD}, hard processes, are accompanied by additional, predominantly low transverse momentum (p_{T}), particles from the proton break-up (beam remnants) and possibly further scatterings, termed Multiple Parton Interactions (MPI) [1]. This associated particle production represents an important background to most observables at hadron colliders and its detailed understanding and modeling with Monte Carlo (MC) generators is crucial for precision measurements and for connecting experimental observables to theory. The empirical models for the description of the non-perturbative aspects in a high-energy scattering event evolution do not allow to clearly separate particles originating from hard processes and the associated event activity event-by-event. In order to enable experimental studies and model comparisons one commonly separates the kinematic region containing the direct fragmentation products of the partons produced in the hardest scattering from the remaining part,

generally referred to as the Underlying Event (UE). The UE also contains particles from initial- and final-state radiation related to the hard interaction.

The first study of this kind was performed by the UA1 experiment at CERN's proton-antiproton (SpS) collider by measuring the transverse energy density outside the leading jet cone [2–4], the so-called jet pedestal region. In the method introduced by CDF [5] and used in the present analysis, one identifies the leading jet, or any other leading object in the event, and measures particle production in the azimuthal region orthogonal to the direction of this leading object, the Transverse region. Based on this method, several UE studies at the Tevatron [5–8] and at the LHC [9–13], at various center-of-mass energies ($\sqrt{s}$), have been published. These also include UE measurements in Drell-Yan [14] and Z-boson [15–17] events performed by CMS and ATLAS.

A common characteristic of UE measurements at all collision energies is that the particle density in the Transverse region as a function of the p_{T} of the leading object ($p_{\mathrm{T}}^{\mathrm{leading}}$) rises steeply at low $p_{\mathrm{T}}^{\mathrm{leading}}$ until a plateau at about twice the inclusive particle density is reached [2]. In the framework of MPI-based models, the probability for a hard scattering increases with the matter overlap in the collisions (decreasing pp impact parameter). And conversely, requiring a high-p_{T} object to be detected in a given collision biases the selection of collisions towards those with a smaller impact parameter, at which the probability for additional uncorrelated scatterings and consequently the charged-particle number-density is enhanced [18]. The charged-particle number-density ($\mathrm{d}N_{\mathrm{ch}}/\mathrm{d}\eta$) in the plateau region increases logarithmically with $\sqrt{s}$ and faster than in minimum-bias events [11]. In MPI-based models, the height of the plateau is sensitive to the pp impact parameter dependence of the number of MPI per event [18]. Hence, UE measurements have facilitated the implementation and tuning of such models [18–21]. They have been used as tools for high precision Standard Model (SM) measurements as well as searches for physics beyond the SM. In recent years it has been shown that they are also important to obtain a qualitative understanding of the centrality dependence of hard processes in p-Pb [22] and Pb-Pb [23, 24] collisions at LHC energies.

During the last decade, the study of the bulk properties of pp collisions has gained increased interest as a research field in its own right. One of the most important discoveries in pp collisions at the LHC is the observation of collective, fluid-like features. They are strikingly similar to those observed in heavy-ion collisions (AA), where they are attributed to the production of a deconfined hot and dense medium, known as the Quark-Gluon Plasma (see ref. [25] for a recent review). The question arises whether the conditions created in high-multiplicity pp collisions can also modify, as in AA [26, 27], the yields of hard probes, for example through partonic energy loss [28]. Hence, the study of hard processes as a function of the charged-particle number-density has moved into the focus of interest. In this context the UE activity in the Transverse region (particle or summed-p_{T} density) provides an event-activity classifier with reduced sensitivity to the hard process studied, which compared to inclusive classifiers can reduce trivial auto-correlation effects [29, 30]. With this in mind, the measurement of the distribution of the number-density in the Transverse region normalized to its average (relative transverse activity, R_{T}) [29] is included in the set of UE measurements reported in this paper.

JHEP04(2020)192

This paper reports measurements characterizing the UE associated with hard scatterings performed at midrapidity ($|\eta| < 0.8$) in pp collisions at $\sqrt{s} = 13$ TeV based on the CDF method [5], which utilizes the leading-charged particles. It extends the previous measurement of the number-density and summed-p_{T} densities using charged particles [13] to a lower p_{T} threshold, $p_{\mathrm{T}}^{\mathrm{track}} > 0.15$ GeV/c, in order to get higher sensitivity to the soft part of the UE. The results are compared to the previous ALICE measurements in the same kinematic regions for pp collisions at $\sqrt{s} = 0.9$ and 7 TeV. The plateau in the Transverse region ($5 < p_{\mathrm{T}}^{\mathrm{leading}} < 40$ GeV/c) is further characterized by the probability distribution of its charged-particle number-density normalized to its average value (R_{T}). Moreover, the mean-transverse momentum in the Transverse region is studied as a function of R_{T}.

The paper is organized as follows: Section 2 introduces the UE observables. The MC event generators used in this paper are described in section 3. The ALICE subsystems used in the analysis are described in section 4, and section 5 is dedicated to the analysis and data correction procedures, which includes the evaluation of the systematic uncertainties. The final results are presented and discussed in section 6 and the conclusions are summarized in section 7.

2 Underlying event observables

The UE observables considered in this study are based on primary charged particles[1] reconstructed in the pseudorapidity range $|\eta| < 0.8$ with three different thresholds of the transverse momentum: $p_{\mathrm{T}}^{\mathrm{track}} > 0.15$, 0.5, and 1.0 GeV/c, for both the leading particle and the associated particles used in the correlation studies. The UE observables are measured in three different regions defined by the relative azimuthal angle, $|\Delta\varphi| = \varphi - \varphi_{\mathrm{leading}}$, to the direction of the leading-charged particle (see figure 1):

- $|\Delta\varphi| < 60°$, the Toward region,
- $60° < |\Delta\varphi| < 120°$, the Transverse region,
- $|\Delta\varphi| > 120°$, the Away region.

The following observables, measured as a function of $p_{\mathrm{T}}^{\mathrm{leading}}$, are considered to characterize the UE:

- average charged-particle density:

$$\frac{1}{\Delta\eta \times \Delta\varphi} \frac{1}{N_{\mathrm{ev}}(p_{\mathrm{T}}^{\mathrm{leading}})} N_{\mathrm{ch}} \tag{2.1}$$

- average summed-p_{T} density:

$$\frac{1}{\Delta\eta \times \Delta\varphi} \frac{1}{N_{\mathrm{ev}}(p_{\mathrm{T}}^{\mathrm{leading}})} \sum p_{\mathrm{T}} \tag{2.2}$$

[1] A primary particle is a particle with a mean proper lifetime τ larger than 1 cm/c, which is either produced directly in the interaction, or from decays of particles with τ smaller than 1 cm/c, restricted to decay chains leading to the interaction [31].

JHEP04(2020)192

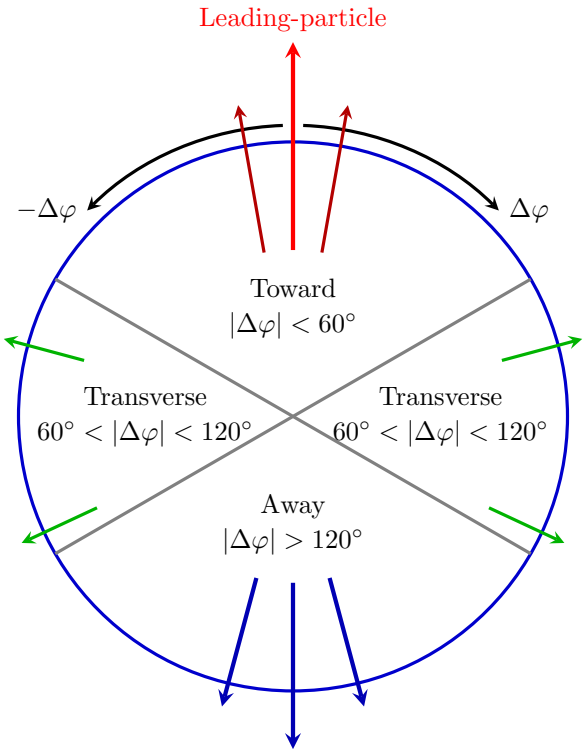

Figure 1. Illustration of the Toward, Transverse, and Away regions in the azimuthal plane with respect to the leading particle direction.

evaluated in the three azimuthal regions, where $N_{\mathrm{ev}}(p_{\mathrm{T}}^{\mathrm{leading}})$ is the number of events satisfying a given $p_{\mathrm{T}}^{\mathrm{leading}}$ interval, $\Delta\varphi = 2\pi/3$ is the width of the regions in azimuth, and $\Delta\eta = 1.6$ is the acceptance window in pseudorapidity. The leading particle is not included in the calculation of the particle density and in the summed p_{T} of the Toward region.

The $p_{\mathrm{T}}^{\mathrm{leading}}$ can be regarded as a suitable proxy for the transverse-momentum scale of the hard scattering to avoid any problems related to jet reconstruction at low transverse momentum. The restriction of the leading-particle pseudorapidity to the acceptance of the detector is part of the definition of the observables. In particular, the measurements did not correct for the fact that particles with $p_{\mathrm{T}} > p_{\mathrm{T}}^{\mathrm{leading}}$ can be present outside the acceptance. Therefore, the same selection is also applied in MC simulations.

The Toward and Away regions are predominated by particle production from the hard process and are, therefore, relatively insensitive to the softer UE. Conversely, the Transverse region is more sensitive to the UE as this region is least affected by contributions from the hardest scattering [5]. Observables defined inside this region are the primary focus of UE measurements.

For $p_{\mathrm{T}}^{\mathrm{leading}}$ above the onset of the jet pedestal plateau, the UE depends only weakly on this quantity. It has therefore been proposed in [29] to study the UE properties in events that contain one leading object with $p_{\mathrm{T}}^{\mathrm{leading}}$ in the range of the plateau, as functions of a

JHEP04(2020)192

new variable for quantifying event activity, relative transverse activity, R_{T}, defined as:

$$R_{\mathrm{T}} = \frac{N_{\mathrm{inc}}}{\langle N_{\mathrm{inc}} \rangle}, \tag{2.3}$$

where N_{inc} is the inclusive number of charged particles in an event and $\langle N_{\mathrm{inc}} \rangle$ is the event-averaged number-density, both evaluated in the Transverse region. Using this observable as an event classifier one can, as proposed in [29], test whether events with very small UE activity are compatible with equivalent measurements in e^+e^- collisions (jet universality) or whether the scaling behaviour towards high UE activity exhibits properties of non-trivial soft-QCD dynamics. As a self-normalized observable, R_{T} is relatively insensitive to center-of-mass energy and kinematic selection variations, while simultaneously covering a large dynamic range in terms of event activity. The present paper reports the first measurement of the R_{T} probability distribution and the mean transverse momentum $\langle p_{\mathrm{T}} \rangle$ in the Transverse region as a function of R_{T}.

3 Monte Carlo models

Particle production in hadronic collisions can be classified according to the energy scale of the process involved. At high-momentum transfers, $Q^2 \gg \Lambda^2_{\mathrm{QCD}}$, perturbative Quantum Chromodynamics (pQCD) is the appropriate theoretical framework to describe partonic interactions. This approach can be used to quantify parton yields and correlations, whereas the transition from partons to hadrons (hadronization) is a non-perturbative process that has to be treated using phenomenological approaches. For momenta of the order of the QCD scale, $\sim 200\,\mathrm{MeV/c}$, a perturbative treatment is no longer feasible. Furthermore, at the center-of-mass energies of the LHC, with momentum transfers of a few GeV/c, the calculated QCD cross sections for $2 \to 2$ parton scatterings exceed the total hadronic cross section for pp collisions (see for example [19]). This suggests that hard MPI occur in this regime. The overall event dynamics cannot be derived fully from first principles and must be described using phenomenological models implemented as general purpose MC generators. In these event generator implementations, model-specific choices are made to regulate these processes at low momentum scales. This section reviews relevant features of the PYTHIA 8 [32] and EPOS [33] MC event generator models, which are used in this study for data correction and for comparison to our fully corrected results. A more detailed description of different general-purpose MC generators can be found for example in [34].

PYTHIA 8. In PYTHIA, event generation starts with a primary process that defines the nature of the event. At LHC energies, this is in most cases a leading order pQCD partonic scattering. At small p_{T} values, color screening effects need to be taken into account. Therefore a cut off, $p_{\mathrm{T},0}$, is introduced, which damps the QCD cross section for $p_{\mathrm{T}} \ll p_{\mathrm{T},0}$. This cut off is one of the main tunable model parameters. Subsequent partonic processes calculable in pQCD are initial- and final-state radiation interleaved with MPI, and the structure of beam remnants. The number of MPI in this model depends on the impact parameter of the pp collision. After these steps, a realistic partonic structure including jets and UE activity is obtained. The partonic configuration is hadronized using

JHEP04(2020)192

string fragmentation as described by the Lund string model [35], followed by the decays of unstable particles. In collisions with several MPI, individual long strings connected to the remnants are replaced by shorter additional strings connecting partons from different MPIs. This mechanism, called color reconnection, has been introduced to reproduce the increase of the average transverse momentum with multiplicity observed in data [36]. For the comparison with measured observables, MC simulated samples with Monash-2013 [37] tune and NNPDF2.3 LO PDF set [38] are used.

Epos LHC. The EPOS [39] event generator can be used to simulate pp, pA, and AA collisions. The multiple scattering approach in EPOS is based on a combination of Gribov-Regge theory and pQCD [33]. An elementary scattering corresponds to a parton ladder, containing a hard scattering calculable based on pQCD, including initial- and final-state radiation. Parton ladders which are formed in parallel to each other share the total collision energy leading to a consistent treatment of energy conservation in hadronic collisions. String hadronization in EPOS is based on the local density of string segments per unit volume with respect to a critical-density parameter. Event-by-event, string segments in low-density regions hadronize normally and independently, creating the corona, while string segments in high-density regions are used to create a core with collective expansion and hadronization including radial and longitudinal flow effects. The EPOS LHC tune considered here is based on a dedicated parameter set used to describe data from all LHC energies and collision systems [40].

4 Experimental setup

ALICE is the dedicated heavy-ion experiment at the LHC. A detailed description of the ALICE detectors can be found in [41]. In the following, only the detector components used in the data analysis presented here are described.

The ALICE apparatus comprises a central barrel (pseudorapidity coverage $|\eta| < 0.9$ over full azimuth) situated in a uniform 0.5 T magnetic field along the beam axis (z) supplied by a large solenoid magnet. The forward and backward rapidity plastic scintillator counters, V0A and V0C, are positioned on each side of the interaction point, covering pseudorapidity ranges $2.8 < \eta < 5.1$ and $-3.7 < \eta < -1.7$, respectively. And they are used for determination of the interaction trigger and to suppress beam-gas and beam-halo background events. The central barrel contains a set of tracking detectors: a six-layer high-resolution silicon Inner Tracking System (ITS) surrounding the beam pipe, and a large-volume (5 m length, 0.85 m inner radius and 2.8 m outer radius) cylindrical Time Projection Chamber (TPC).

The first two layers of the ITS are equipped with high-granularity Silicon Pixel Detectors (SPD), which cover the pseudorapidity ranges $|\eta| < 2.0$ and $|\eta| < 1.4$ respectively. The position resolution is 12 μm in r-φ and about 100 μm along the beam direction. The following two layers are composed of Silicon Drift Detectors (SDD). The position along the beam direction is measured via collection anodes, and the associated position resolution is about 50 μm. The r-φ coordinate is given by a drift-time measurement, with a spatial

JHEP04(2020)192

resolution of about 60 μm. Finally, the two outer layers are made of double-sided Silicon micro-Strip Detectors (SSD) with a position resolution of 20 μm in r-φ and about 800 μm along the beam direction. The material budget of all six layers, including support and services, amounts to 7.7% of a radiation length in the transverse plane.

The TPC covers the pseudorapidity range of about $|\eta| < 0.9$ for tracks traversing the outer radius. In order to avoid border effects, the fiducial region has been restricted in this analysis to $|\eta| < 0.8$. The position resolution along the r-φ coordinate varies from 1100 μm at the inner radius to 800 μm at the outer. The resolution along the beam axis ranges from 1250 μm to 1100 μm.

The ITS and TPC space points are combined to reconstruct tracks from charged particles over a wide transverse momentum range starting from $p_{\mathrm{T}} = 0.15$ GeV/c. The tracking efficiency estimated from a full simulation of the detectors is $\approx 65\%$ at the lowest p_{T}, and increases with p_{T}, plateauing at $\approx 80\%$ for $p_{\mathrm{T}} > 2$ GeV/c. The transverse momentum resolution is better than 3% for primary tracks below 1 GeV/c, and degrades linearly up to 6% at $p_{\mathrm{T}} = 40$ GeV/c [42]. The transverse impact parameter resolution decreases from 300 μm at 0.2 GeV/c to 20 μm at 30 GeV/c.

5 Analysis procedure

5.1 Event selection

The measurements presented here use data collected by ALICE during the 2016 LHC pp run at $\sqrt{s} = 13$ TeV. During this period, minimum-bias (MB) events were selected using the high purity V0-based MBand trigger which required a charged-particle signal coincidence in the V0A and V0C arrays. It is the same trigger as used in LHC Run 1 high-luminosity data taking [42]. After event selection, a data sample of 46.2 million MBand triggered events is obtained. Further event selection for offline analysis is made by requiring a primary vertex position along the z-axis within ± 10 cm ($|v_z| < 10$ cm) around the nominal interaction point to ensure full geometrical acceptance in the ITS. Pile-up interactions are limited by keeping the average number of pp interactions per bunch crossing below 0.06 through beam separation in the horizontal plane. Residual pile-up events are rejected based on a multiple interaction points finding algorithm using SPD information [42]. Primary tracks satisfying various quality selection criteria, described in the next section, are used in this analysis. Moreover, at least one track with a minimum transverse momentum $p_{\mathrm{T}}^{\mathrm{track}} = 0.15$, 0.5, and 1.0 GeV/$c$ in the acceptance range $|\eta| < 0.8$ is required for the analysis. Table 1 summarizes the percentage of events remaining after each event selection step for the various $p_{\mathrm{T}}^{\mathrm{track}}$ selections. The last row in the table shows the sample size available for the R_{T} analysis.

5.2 Track selection

The selected charged-particle tracks are required to have at least 70 TPC space points, the number of geometrically possible clusters which can be assigned to a track, and more than 60% of the findable TPC space points, i.e. those that can be assigned to tracks based on geometrical criteria derived from track parameters. The track selection criteria

JHEP04(2020)192

	Events	Fraction (%)
Offline trigger	46.2 M	100.0
Reconstructed vertex	42.8 M	92.6
$p_{\mathrm{T}}^{\mathrm{track}} > 0.15$ GeV/c	40.4 M	87.4
$p_{\mathrm{T}}^{\mathrm{track}} > 0.5$ GeV/c	34.5 M	74.7
$p_{\mathrm{T}}^{\mathrm{track}} > 1.0$ GeV/c	22.1 M	47.8
$p_{\mathrm{T}}^{\mathrm{leading}} > 5.0$ GeV/c	0.43 M	0.93

Table 1. Events (absolute numbers and percentages) remaining after each event selection step.

are optimized for good momentum resolution and minimal contamination from secondary tracks. For this purpose a track must have at least 3 clusters in the ITS, one of which has to be in the first 3 layers. The quality of the track fitting measured in terms of the χ^2 per space point is required to be lower than 4 (each space point having 2 degrees of freedom). Moreover, to reject secondary tracks, the distance of closest approach (DCA) of the track to the primary vertex along the beam axis (DCA_Z) is required to be smaller than 2 cm. In the transverse direction, the maximum allowed DCA_{XY} corresponds to seven times the p_{T}-dependent DCA_{XY} resolution.

5.3 Corrections

For efficiency and acceptance corrections, events are generated with the PYTHIA 8 MC with the same tune as listed in the early section. They are subsequently transported through the software description of the ALICE apparatus using GEANT 3.21 [44]. For particles crossing sensitive detector layers the detector response is simulated. The simulated events are reconstructed and analyzed using the same algorithms as used for the real data. The number of simulated events similar to the ones in data are used to determine the corrections.

The measured particle and $\sum p_{\mathrm{T}}$ densities are corrected for tracking efficiency, contamination from secondary particles, and the finite vertex reconstruction efficiency. The particle with the highest p_{T} in a collision may not be detected due to finite acceptance and efficiency of the detection apparatus, and a lower p_{T} track enters the analysis instead. If the misidentified leading particle has a different p_{T} but roughly the same direction as the true leading particle, this leads to a shift in $p_{\mathrm{T}}^{\mathrm{leading}}$. On the other hand, if the misidentified leading particle has a significantly different direction than the true one, this will cause a rotation of the event topology and a bias on the UE observables. The data are corrected for these effects using a data-driven procedure described in detail in ref. [11].

Table 2 summarizes the maximum effect of each correction on the measured final observable for $p_{\mathrm{T}}^{\mathrm{track}} > 0.15$ GeV/c. For other $p_{\mathrm{T}}^{\mathrm{track}}$ thresholds the effects are similar. The correction procedures follow the same approach as described in [11]. In the following only the corrections for R_{T}-related distributions using unfolding and re-weighting methods will be detailed.

Correction	**charged-particle density**	$\sum p_{\mathrm{T}}$ **density**
Efficiency	30%	25%
Leading track misidentification	7%	7%
Contamination	3%	2%
Vertex reconstruction	0.9%	0.9%

Table 2. Maximum effect of p_{T}-dependent corrections on measured particle and summed-p_{T} densities with $p_{\mathrm{T}}^{\mathrm{track}} > 0.15$ GeV/c threshold.

Due to the finite momentum resolution and tracking efficiency of the detector, the measured R_{T} probability distribution and the charged-particle $\langle p_{\mathrm{T}} \rangle$ distribution as a function of R_{T} are distorted. This affects, in particular, the R_{T} probability distribution which falls steeply at large R_{T}. For this reason an unfolding procedure is employed to correct for detector effects. For the measurement of the charged-particle $\langle p_{\mathrm{T}} \rangle$ vs. R_{T} both quantities have to be corrected. For the full unfolding a 4-dimensional response matrix is needed. Considering that the charged-particle $\langle p_{\mathrm{T}} \rangle$ rises slowly as a function of R_{T}, a re-weighting correction procedure is performed, as described in [45, 46].

Unfolding. The R_{T} probability distribution is corrected using 1-dimensional Bayesian unfolding [47], an iterative method based on Bayes' theorem, as implemented in the RooUnfold package [48]. To this end, a 2-dimensional response matrix is created using the PYTHIA 8 generator. It maps the particle level $R_{\mathrm{T}}^{\mathrm{truth}}$ obtained from a MC simulation to the detector level $R_{\mathrm{T}}^{\mathrm{meas}}$ obtained after full GEANT3 based transport, track reconstruction, and track selection. Projections of the distribution of $R_{\mathrm{T}}^{\mathrm{meas}}$ for a given $R_{\mathrm{T}}^{\mathrm{truth}}$ are well approximated by a Gaussian distribution, and hence, described by its mean and standard deviation. This is used to extrapolate the response matrix into a region where statistical uncertainties are large and can deteriorate the quality of the unfolding. Figure 2 shows the mean and standard deviation of $R_{\mathrm{T}}^{\mathrm{meas}}$ as a function of $R_{\mathrm{T}}^{\mathrm{truth}}$ obtained from the PYTHIA 8 simulation. A linear function and a function of the form $a\sqrt{x} + b$ are used to fit the mean and the standard deviation, respectively. Over the whole $R_{\mathrm{T}}^{\mathrm{truth}}$ range the relative difference between the fit and the simulated data is less than 1% and less than 0.2% for $R_{\mathrm{T}}^{\mathrm{truth}} < 2$. Therefore, the results of the fits are used to extend the response matrix to $R_{\mathrm{T}}^{\mathrm{truth}} > 2$. The smoothened response matrix is used for R_{T} probability distribution unfolding and $\langle p_{\mathrm{T}} \rangle$ re-weighting, with the difference between the data points and the parameterized fitting functions (as shown in figure 2) being propagated to the final systematical uncertainties.

For the unfolding correction, the PYTHIA 8 generated $R_{\mathrm{T}}^{\mathrm{truth}}$ distribution is used as the prior. Convergence is reached typically after three iterations. As an additional cross check, the analysis is also carried out using the Singular Value Decomposition (SVD) un-

JHEP04(2020)192

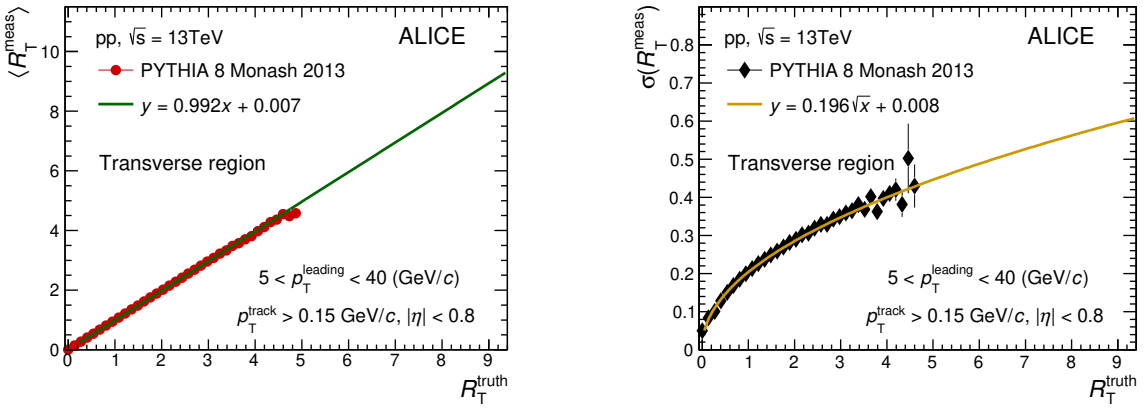

Figure 2. Mean $R_{\mathrm{T}}^{\mathrm{meas}}$ and standard deviation σ of the $R_{\mathrm{T}}^{\mathrm{meas}}$ distribution as a function of $R_{\mathrm{T}}^{\mathrm{truth}}$. The solid lines represent the fits to the points and the extrapolation to higher $R_{\mathrm{T}}^{\mathrm{truth}}$, resulting in the parameterized response matrix used for unfolding.

folding [49]. The relative difference between the SVD and Bayesian unfolded distributions is found to be below 2%. To study the influence of the corrections using a particular MC event generator, EPOS LHC generator is also used to determine the unfolding response matrix and as prior in the unfolding process. The difference of the unfolded results using different MC generator corrections is considered as part of unfolding uncertainty.

Mean p_{T} re-weighting. For the measurement of the charged-particle $\langle p_{\mathrm{T}} \rangle$ as a function of R_{T}, a re-weighting approach is used. The procedure is implemented based on the following relation between the true and measured R_{T}

$$\langle p_{\mathrm{T}} \rangle (R_{\mathrm{T}}^{\mathrm{truth}}) = \sum P(R_{\mathrm{T}}^{\mathrm{meas}} | R_{\mathrm{T}}^{\mathrm{truth}}) \times \langle p_{\mathrm{T}} \rangle (R_{\mathrm{T}}^{\mathrm{meas}}) \tag{5.1}$$

where $P(R_{\mathrm{T}}^{\mathrm{meas}} | R_{\mathrm{T}}^{\mathrm{truth}})$ is the normalised probability distribution of $R_{\mathrm{T}}^{\mathrm{meas}}$ in a given $R_{\mathrm{T}}^{\mathrm{truth}}$ interval, which is obtained from the detector response matrix previously described.

5.4 Systematic uncertainties

The evaluation of the systematic uncertainties on the charged-particle number density and $\sum p_{\mathrm{T}}$ density follows closely the methods developed for inclusive charged-particle measurements [45, 50, 51] and the UE measurements at lower collision energies [11]. Table 3 summarizes the systematic uncertainties evaluated for the particle transverse momentum $p_{\mathrm{T}}^{\mathrm{track}} > 0.15$ GeV/c threshold, for selected $p_{\mathrm{T}}^{\mathrm{leading}}$ ranges. In the following, the individual sources of systematic uncertainty, listed in the first column of table 3, will be described briefly. A detailed description of the procedures can be found in [11].

- *ITS-TPC track matching efficiency:* systematic uncertainties on the ITS and TPC detector efficiencies are estimated by comparing the experimental ITS-TPC track matching efficiencies with those obtained using the MC sample.

- *Track and vertex selection:* by applying the efficiency and contamination corrections, one accounts for those particles which are lost due to detector effects, vertex

JHEP04(2020)192

	Charged-particle density		Summed-p_{T} density	
	$p_{\mathrm{T}}^{\mathrm{leading}} < 1$ GeV/c	$p_{\mathrm{T}}^{\mathrm{leading}} > 6$ GeV/c	$p_{\mathrm{T}}^{\mathrm{leading}} < 1$ GeV/c	$p_{\mathrm{T}}^{\mathrm{leading}} > 6$ GeV/c
ITS-TPC track matching	0.3%	2.3%	0.4%	3.2%
Track cuts	0.8%	1.6%	0.7%	1.5%
Secondaries contamination	0.2%	0.2%	0.2%	0.2%
Misidentification bias	0.7%	negligible	0.9%	negligible
Vertex reconstruction	0.3%	negligible	0.3%	negligible
MC non-closure	0.9%, 0.9%, 1.1%	0.7%, 0.1%, 0.1%	0.4%, 0.2%, 0.4%	0.6%, 0.3%, 0.3%
MC dependence	0.3%, 0.6%, 0.8%	1.7%, 2.8%, 2.8%	0.5%, 0.5%, 0.4%	1.0%, 3.0%, 3.0%
Total uncertainty	1.5%, 1.5%, 1.8%	3.4%, 3.9%, 3.9%	1.4%, 1.4%, 1.5%	3.9%, 4.7%, 4.6%

Table 3. Systematic uncertainties of the charged-particle number and summed-p_{T} densities as a function of $p_{\mathrm{T}}^{\mathrm{leading}}$ for the transverse momentum threshold $p_{\mathrm{T}}^{\mathrm{track}} > 0.15$ GeV/c in pp collisions at $\sqrt{s} = 13$ TeV. When more than one number is quoted, the values refer to the uncertainty in Toward, Transverse, and Away regions, respectively; they are independent of the azimuthal region in all other cases.

reconstruction inefficiency, and secondary tracks which have not been removed by the selection criteria. These corrections rely on detector simulations. Therefore, the systematic uncertainties were estimated by varying the choices of track parameter requirements and vertex reconstruction parameters.

- *Secondary particle contamination:* MC generators underestimate the production of strange particles in data. The effect on the secondary particle contamination correction was estimated by varying the strange particle fraction between the one given by PYTHIA and the one compatible with the tails of the DCA_{XY} distribution which are predominantly populated by secondaries.

- *Misidentification bias:* the uncertainty on the leading-track misidentification correction is estimated from the discrepancy between a data-driven correction used in the analysis and an alternative method based on simulations.

- *MC non-closure:* by correcting an MC generator prediction after full detector simulation with corrections extracted using the same generator, one expects to reproduce the input MC prediction within statistical uncertainty. This consideration holds true only if each correction is evaluated with respect to all the variables to which the given correction is sensitive. Any statistically significant difference between input and corrected distributions is referred to as MC non-closure and is added in quadrature to the total systematic uncertainty.

- *MC dependence:* the difference in final distributions when applying corrections extracted using PYTHIA 8 or EPOS LHC generators was quantified and added to the systematic uncertainty.

JHEP04(2020)192

Since R_{T} is a self-normalized quantity evaluated event-by-event, the systematic uncertainties related to the ITS-TPC track matching efficiency and track cuts partially cancel each other. A residual effect results from the fact that the p_{T} spectrum gets harder with increasing multiplicity, leading to a difference between the p_{T} weighted efficiencies for N_{inc} and $\langle N_{\mathrm{inc}} \rangle$, which is imperfectly accounted for through the MC-based response matrix. The resulting scale uncertainty on R_{T} has been estimated by varying the shape of the p_{T} spectra within uncertainties taken from the spectrum analysis [51]. The variations are propagated to the R_{T} distribution via the response matrix.

Another contribution to the systematic uncertainty on the R_{T} distribution results from the event selection. This uncertainty is estimated by repeating the R_{T} analysis using a more restrictive selection on the primary vertex, $|v_z| < 7$ cm. Since the vertex reconstruction efficiency increases with N_{inc}, also the systematic uncertainty related to this efficiency cancels only partially in the ratio N_{inc} / $\langle N_{\mathrm{inc}} \rangle$ (in particular at low N_{inc}, where the efficiency is low). This uncertainty is evaluated by changing the default selection from one minimum track contributing to the primary vertex to two tracks. The resulting difference of 2.7% is assigned as the systematic uncertainty on the N_{inc} determination.

To validate the unfolding procedure, and identify potential biases, closure tests are performed which compare the unfolded distribution to the particle-level truth in the MC simulation. Consistency of the unfolding procedure is also ensured by re-folding the solution to detector level and comparing it to the uncorrected distribution used as input. The remaining difference of 0.3% is assigned as uncertainty from MC non-closure. As discussed in the previous section, the Bayesian unfolding is employed as the default method. The number of iterations serves as a regularization parameter in Bayesian unfolding. Based on the closure test and convergence, four iterations were chosen as the default. To estimate the related systematic uncertainty, the iterations parameter is varied by ± 2. The unfolded results are quite stable against regularization parameter variations with a maximum deviation of 1.2% at high-R_{T}. As an independent cross-check, the SVD unfolding has also been used in the analysis and the difference between SVD and Bayesian unfolded results are found to be less than 0.4%. The corrected R_{T} distribution is obtained after the unfolding, which is performed using the detector response matrix computed based on simulations with PYTHIA 8 tune Monash-2013. This particular choice of MC event generator affects the prior used for unfolding. To investigate the systematic uncertainty from this particular choice, the prior distributions are varied using the deviations of fitted Negative Binomial Distribution (NBD) distribution (see section 6).

For the measurement of the $\langle p_{\mathrm{T}} \rangle$ distribution vs. R_{T}, a 1% systematic uncertainty from MC non-closure using the re-weighting procedure is assigned. The uncertainty from the ITS-TPC track matching efficiency contributes to 1.3%, while the track selection criteria results in a total uncertainty of around 0.4%. The residual scale uncertainty due to the particle p_{T}-spectrum slope changes is estimated using the same approach as described for R_{T}. Here both R_{T} and $\langle p_{\mathrm{T}} \rangle$ are affected and therefore the residual scale uncertainty largely cancels out, resulting in a systematic uncertainty of 0.2% on $\langle p_{\mathrm{T}} \rangle$. The variations of the number of vertex contributors and the vertex cut contribute both 0.2 % to the systematic uncertainty.

JHEP04(2020)192

	R_{T} probability distribution	$\langle p_{\mathrm{T}} \rangle$ vs. R_{T}
Unfolding	± 3.1%	—
Z vertex cut	± 2.4%	± 0.2%
Minimum of N_{ch} to primary vertex	± 2.7%	± 0.2%
Track cuts	—	± 0.4%
ITS-TPC track matching	—	± 1.3%
Residual scale	± 2.2%	± 0.2%
MC non-closure	± 0.4%	± 1.0%
Total uncertainty	± 5.3%	± 1.6%

Table 4. Systematic uncertainties for R_{T} probability and $\langle p_{\mathrm{T}} \rangle$ distributions as a function of R_{T}.

The maximum systematic uncertainties for the R_{T} probability and $\langle p_{\mathrm{T}} \rangle$ distributions as a function of R_{T} are summarized in table 4. The overall systematic uncertainty is calculated by summing the different contributions in quadrature.

6 Results and discussion

In the following the results for the charged-particle number and summed-p_{T} densities in three azimuthal regions are reported and discussed. Then the results for the R_{T} probability and $\langle p_{\mathrm{T}} \rangle$ vs. R_{T} distributions in the Transverse region are presented. The experimental results are compared to model calculations using PYTHIA 8 and Epos LHC.

6.1 Charged-particle number density N_{ch} and $\sum p_{\mathrm{T}}$ distributions

Figure 3 shows the average charged-particle number and summed-p_{T} densities as a function of $p_{\mathrm{T}}^{\mathrm{leading}}$, in the Toward, Transverse, and Away regions for the transverse momentum threshold requirement of $p_{\mathrm{T}}^{\mathrm{track}} > 0.15$ GeV/c. The averaged charged-particle number and summed-p_{T} densities as a function of $p_{\mathrm{T}}^{\mathrm{leading}}$ using different p_{T} thresholds for the associated particles, $p_{\mathrm{T}}^{\mathrm{track}} > 0.5$ and 1.0 GeV/c, are presented in appendix A. Figure 4 shows the averaged charged-particle number and summed-p_{T} densities as a function of $p_{\mathrm{T}}^{\mathrm{leading}}$ in the Toward, Transverse, and Away regions for the transverse momentum threshold requirement of $p_{\mathrm{T}}^{\mathrm{track}} > 0.15$ GeV/c, and the comparison to MC results. The $p_{\mathrm{T}}^{\mathrm{leading}}$ dependence in all regions show a similar behavior. At low $p_{\mathrm{T}}^{\mathrm{leading}}$, there is a steep rise in event activity followed by a change to a smaller gradient at $p_{\mathrm{T}}^{\mathrm{leading}} \sim 5$ GeV/c, the plateau region. Above this value in the Transverse region, and in particular for the number density, the event activity becomes almost independent of $p_{\mathrm{T}}^{\mathrm{leading}}$, while it continues to rise in the Toward and Away regions.

In the MPI implementation of PYTHIA, the average number of hard scatterings per event depends strongly on the impact parameter. Conversely, tagging hard scatterings with

JHEP04(2020)192

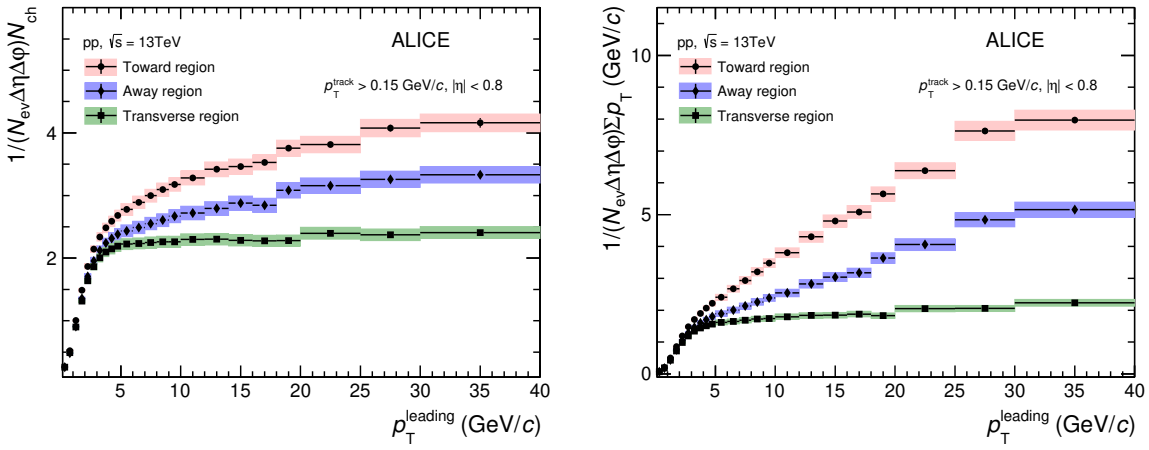

Figure 3. Number density N_{ch} (left) and $\sum p_{\mathrm{T}}$ (right) distributions as a function of $p_{\mathrm{T}}^{\mathrm{leading}}$ in Toward, Transverse, and Away regions for $p_{\mathrm{T}}^{\mathrm{track}} > 0.15$ GeV/c. The shaded areas represent the systematic uncertainties and vertical error bars indicate statistical uncertainties.

high-p_{T} particles biases the events towards lower impact parameter and, hence, higher event activity. The change of slope observed in data corresponds to the transverse momentum where the leading particle is dominantly produced by rare hard scatterings, where the average yield per event for such a process is $\ll 1$. This is plausible, in PYTHIA, since requiring particles with lower $p_{\mathrm{T}}^{\mathrm{leading}}$ which are produced in almost every parton-parton interaction there cannot be a significant bias on the number of MPI. The continuous rise observed for the Toward and Away regions can be attributed to particles not only from the UE but also to the contribution of fragments from hard scatterings, which are mainly back-to-back in azimuth. The contribution from fragments increases with $p_{\mathrm{T}}^{\mathrm{leading}}$ causing the rise of event activity. In contrast, only a small number of fragments enter the Transverse region. In addition to the contributions from MPI uncorrelated with the hardest scattering, this region contains particles originating from initial-state radiation and hard scatterings which produce more than two jets, causing the slow rise of event activity with $p_{\mathrm{T}}^{\mathrm{leading}}$observed in the jet plateau range.

Figure 5 compares the number density and $\sum p_{\mathrm{T}}$ distributions as a function of $p_{\mathrm{T}}^{\mathrm{leading}}$ in the Transverse region for the three threshold selections $p_{\mathrm{T}}^{\mathrm{track}} > 0.15$, 0.5, and 1.0 GeV/c. In the plateau region, increasing the cut from $p_{\mathrm{T}}^{\mathrm{track}} > 0.15$ GeV/c to $p_{\mathrm{T}}^{\mathrm{track}} > 1.0$ GeV/c reduces the number density by almost a factor of 4. The relative slope of the distributions in the pedestal region slightly increases with the $p_{\mathrm{T}}^{\mathrm{track}}$ threshold, indicating an increased contribution of correlated hard processes (initial-state radiation) to the Transverse region. This shows that the highest sensitivity to the UE is obtained using the lowest p_{T} threshold.

Figures 4 and 5 also compare the number density N_{ch} and $\sum p_{\mathrm{T}}$ densities to the results of PYTHIA 8 and EPOS LHC calculations. PYTHIA 8 describes the plateau in the Transverse region quite well, while EPOS LHC underpredicts the densities in this region (as well as in the Toward region) by about 20%. When increasing the $p_{\mathrm{T}}^{\mathrm{track}}$ cut, the agreement between data and PYTHIA 8 in the Toward and Away regions becomes slightly worse (see

JHEP04(2020)192

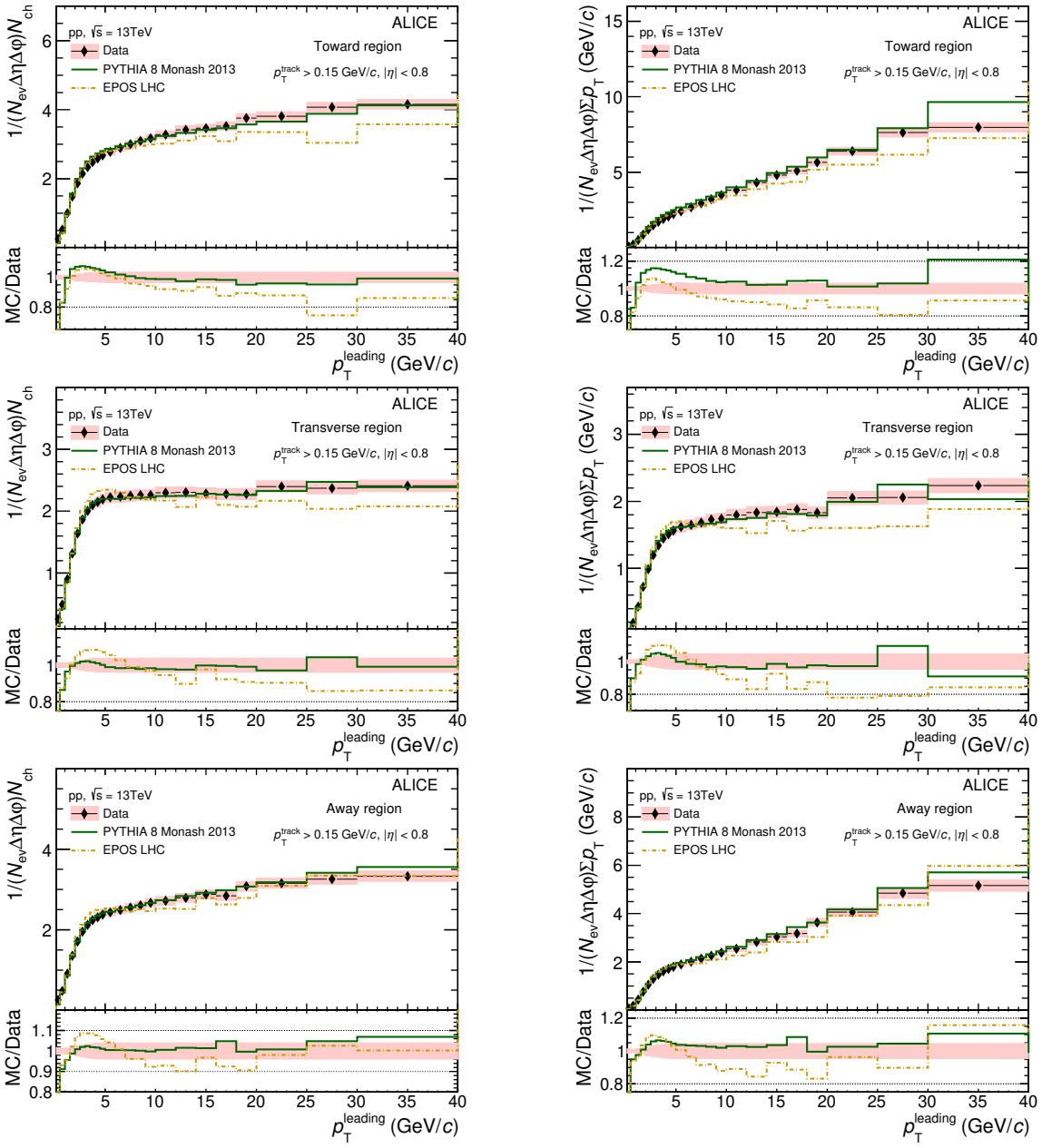

Figure 4. Number density N_{ch} (left) and $\sum p_{\mathrm{T}}$ (right) distributions as a function of $p_{\mathrm{T}}^{\mathrm{leading}}$ along with the MC simulations in Toward (top), Transverse (middle), and Away (bottom) regions for the threshold of $p_{\mathrm{T}}^{\mathrm{track}} > 0.15$ GeV/c. The shaded areas in the upper panels represent the systematic uncertainties and vertical error bars indicate statistical uncertainties for the data. In the lower panels, the shaded areas are the sum in quadrature of statistical and systematic uncertainties from upper panels. No uncertainties are shown for the MC simulations.

JHEP04(2020)192

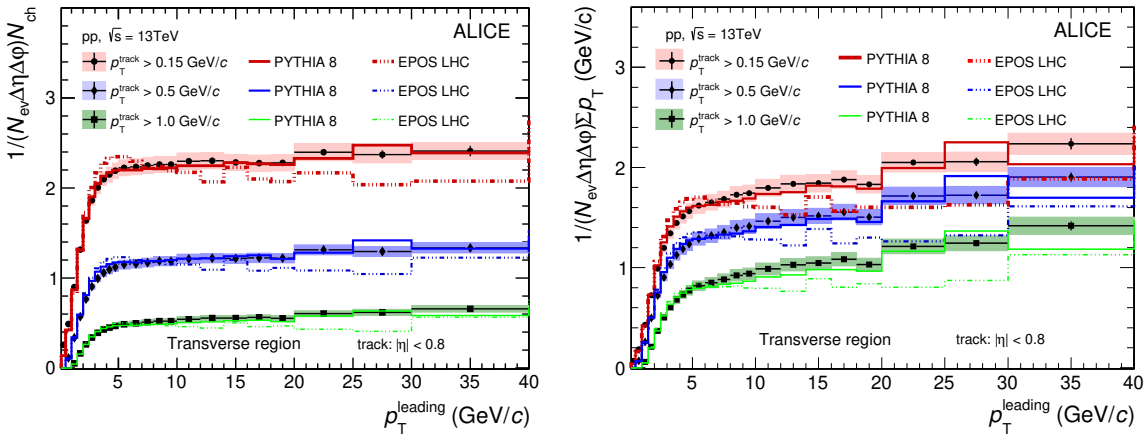

Figure 5. Number density $N_{\rm ch}$ (left) and $\sum p_{\rm T}$ (right) distributions as a function of $p_{\rm T}^{\rm leading}$ along with the MC simulations in Transverse region for three transverse momentum thresholds of $p_{\rm T}^{\rm track} > 0.15$, 0.5, and 1.0 GeV/c. The shaded areas represent the systematic uncertainties and vertical error bars indicate statistical uncertainties for the data. No uncertainties are shown for the MC simulations.

appendix A), with the largest discrepancies appearing at low $p_{\rm T}^{\rm leading}$ in the Toward region. In general Epos LHC fails to reproduce the experimental data in most regions. This can be attributed to the underprediction of the number of hard scatterings in the model. The issue is expected to be solved in EPOS 3 using a new variable saturation scale [52, 53].

Figure 6 (left) shows the comparison of the results obtained at $\sqrt{s} = 13$ TeV to the ones obtained at lower collision energies, $\sqrt{s} = 0.9$ and 7 TeV [11], in the Transverse region. Between the two higher energies, the number density in the plateau increases by about 30%. More information about the $\sqrt{s}$-dependence in the Transverse region can be obtained by comparing the shapes of the number density vs. $p_{\rm T}^{\rm leading}$. To this end, the height of the plateau for different collision energies is quantified by fitting a constant function in the range $5 < p_{\rm T}^{\rm leading} < 10$ GeV/c, shown as lines in figure 6 (left). The fitting range was restricted to the common range in order to be consistent with the procedure used for the measurements at lower $\sqrt{s}$. Larger fitting ranges were also considered and consistent results were obtained. The shapes of the particle densities as a function of $p_{\rm T}^{\rm leading}$ are then compared after dividing the densities by the height of the plateau. The results are shown in figure 6 (right). For the two higher energies the coverage extends beyond the fitting range, i.e. to $p_{\rm T} > 10$ GeV/c. In this range the densities agree within the statistical and systematic uncertainties. In the region of the rise ($p_{\rm T} < 5$ GeV/c) one observes a clear ordering among the three collision energies, the lowest energy having the highest density relative to the plateau. At lower $\sqrt{s}$ the plateau starts at a slightly lower $p_{\rm T}^{\rm leading}$.

Figure 7 shows the $\sqrt{s}$-dependence of the number density of the plateau in the Transverse region for $p_{\rm T}^{\rm track} > 0.5$ GeV/c, from a fitting of a constant function in the $p_{\rm T}^{\rm leading}$ range $5 < p_{\rm T}^{\rm leading} < 10$ GeV/c. The lower energy data are taken from ALICE [11] and CDF [5] measurements. It is compared with the midrapidity charged-particle density $\mathrm{d}N_{\rm ch}/\mathrm{d}\eta|_{\eta=0}$ of charged-particles with $p_{\rm T} > 0.5$ GeV/c in MB events also requiring at least one charged particle in $|\eta| < 2.5$ (scaled by $1/2\pi$) [54]. The UE activity in the plateau

JHEP04(2020)192

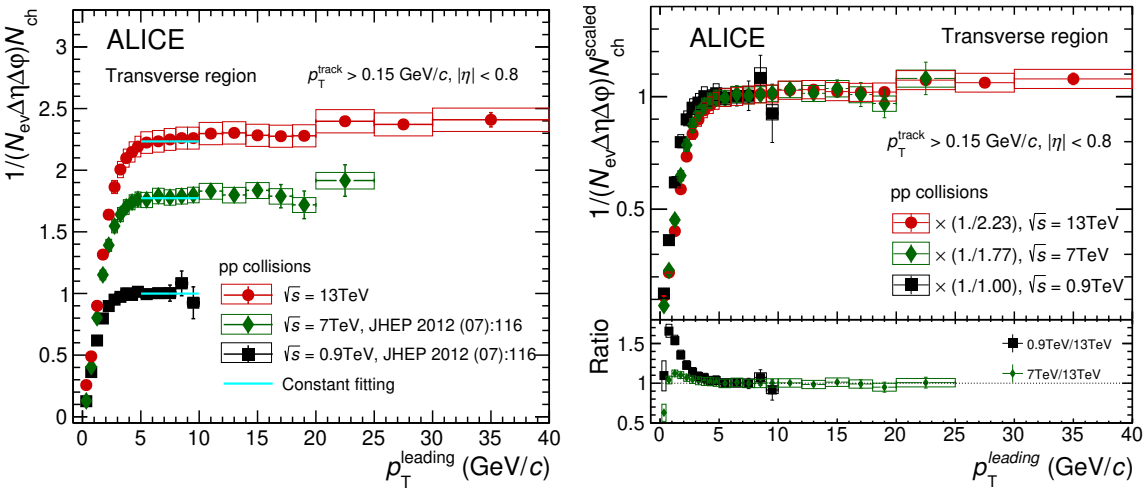

Figure 6. Left: number density $N_{\rm ch}$ in the Transverse region as a function of $p_{\rm T}^{\rm leading}$ ($p_{\rm T}^{\rm track} >$ 0.15 GeV/c threshold) for $\sqrt{s} = 0.9$, 7 and 13 TeV. A constant function is used to fit the data in the range $5 < p_{\rm T}^{\rm leading} <$ 10 GeV/c and the results are shown as solid lines. Right: number densities $N_{\rm ch}$ scaled by the pedestal values obtained from the fit in order to compare the shapes. The open boxes represent the systematic uncertainties and vertical error bars indicate statistical uncertainties.

region is more than a factor of two higher than $\mathrm{d}N_{\rm ch}/\mathrm{d}\eta$. Both are consistent with a logarithmic dependence on collision energy. Between $\sqrt{s} = 0.9$ and 13 TeV $\mathrm{d}N_{\rm ch}/\mathrm{d}\eta$ increases by approximately a factor of 2.1 whereas the increase of the UE activity is 30% larger, confirming the trend observed previously for collision energies up to 7 TeV.

ATLAS has published similar UE results measured in a wider rapidity acceptance of $|\eta| < 2.5$ and using a threshold of $p_{\rm T}^{\rm track} > 0.5$ GeV/c [13]. Since jets have a finite extension in η-φ space, the larger acceptance allows more particles from the leading jet fragmentation and in particular, from the away-side partner jet subject to a pseudorapidity swing, to enter the measurement and, hence, the results in the Toward and Away regions are not directly comparable between the two experiments. Notably, the smaller acceptance obscures an interesting feature observed by ATLAS: for $p_{\rm T}^{\rm leading} > 7$ GeV/c the Away region has a higher charged-particle multiplicity density than the Toward region, despite not containing the highest-$p_{\rm T}$ charged particle. In the ALICE measurement the Toward region has always the higher multiplicity density (see figure 3). However, when comparing the distributions from the Transverse region one observes good agreement (figure 8) in the plateau region. This indicates that the UE activity does not depend strongly on the rapidity coverage and that the fact that in some cases particles with $p_{\rm T} > p_{\rm T}^{\rm leading}$ are outside the acceptance does not have a strong effect on the measurement. For the lower acceptance used in ALICE, the plateau starts at a slightly lower $p_{\rm T}^{\rm leading}$. As a consequence, in the region of the steep rise for $p_{\rm T}^{\rm leading} < 5$ GeV/c, the ratio between the densities for the higher and lower η acceptance increases strongly with $p_{\rm T}^{\rm leading}$. In MPI-based models, like the one implemented in PYTHIA 8, the onset of the plateau is reached when the per-event probability to find a leading particle of a given $p_{\rm T}^{\rm leading}$ is much less than unity. Decreasing the acceptance or, as discussed above, lowering the collision energy would move the onset of the plateau to smaller $p_{\rm T}^{\rm leading}$, which is in agreement with our observations (see PYTHIA 8 comparison in figure 8).

JHEP04(2020)192

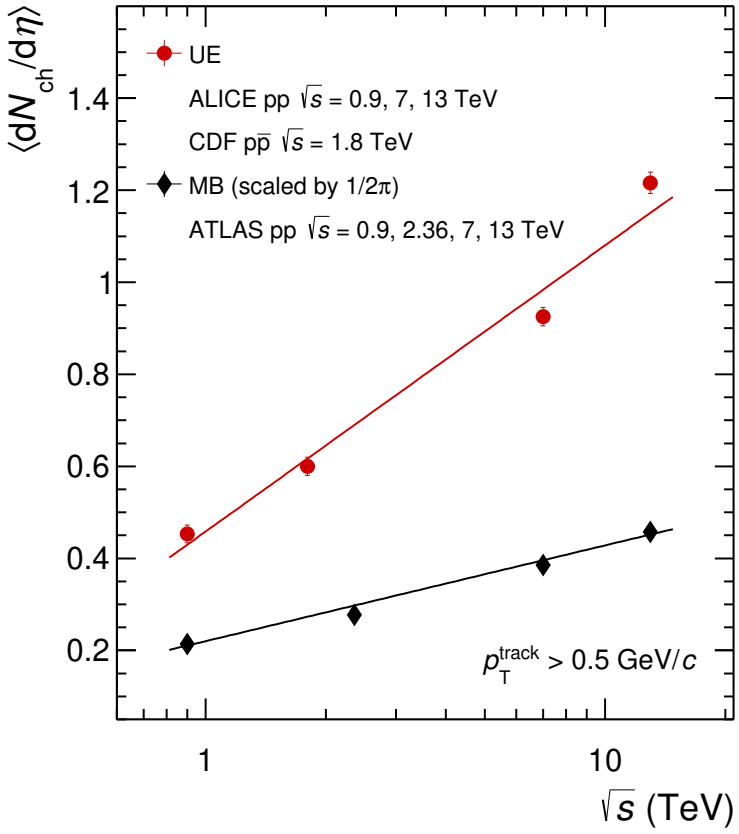

Figure 7. Comparison of number density in the plateau of the Transverse region with lower energy data taken from [5, 11] and $dN_{\text{ch}}/d\eta$ in minimum-bias events (scaled by $1/2\pi$) [54]. Both are for charged-particles with $p_{\text{T}} > 0.5$ GeV/c. Error bars represent statistical and systematic uncertainties summed in quadrature. The straight lines show the results of fitting data points with the functional form $a + b \ln s$.

6.2 Relative transverse activity classifier R_{T} distributions

The R_{T} analysis is performed using a track transverse momentum threshold of $p_{\text{T}}^{\text{track}} > 0.15$ GeV/c and by selecting events in the plateau region ($p_{\text{T}}^{\text{leading}} > 5\,\text{GeV}/c$). Here the R_{T} probability distribution and the mean charged-particle p_{T} as a function of R_{T}, in the Transverse region, are reported.

The R_{T} probability distribution is shown in figure 9. The distribution has been fitted by a modified NBD with the multiplicity scaled by its average value, as was done for the measured R_{T} observable. Within the experimental uncertainties, the NBD fit gives a good description of the data up to $R_{\text{T}} = 3$, and it slightly overestimates the data with increasing R_{T}, by about 14% at $R_{\text{T}} = 5$. The distribution is also compared with the calculations from PYTHIA 8 and EPOS LHC. While both models describe the data well in the R_{T} regions close to the peak at $R_{\text{T}} \sim 0.7$, both PYTHIA 8 and EPOS LHC calculations diverge strongly at higher R_{T}, and underpredict the R_{T} distribution by more than a factor of two for $R_{\text{T}} > 4$. This opens possibilities to study the interplay of components of pp collisions. Detailed MC event generators studies are needed to interpret the mechanisms responsible for the disagreement at high R_{T} values.

JHEP04(2020)192

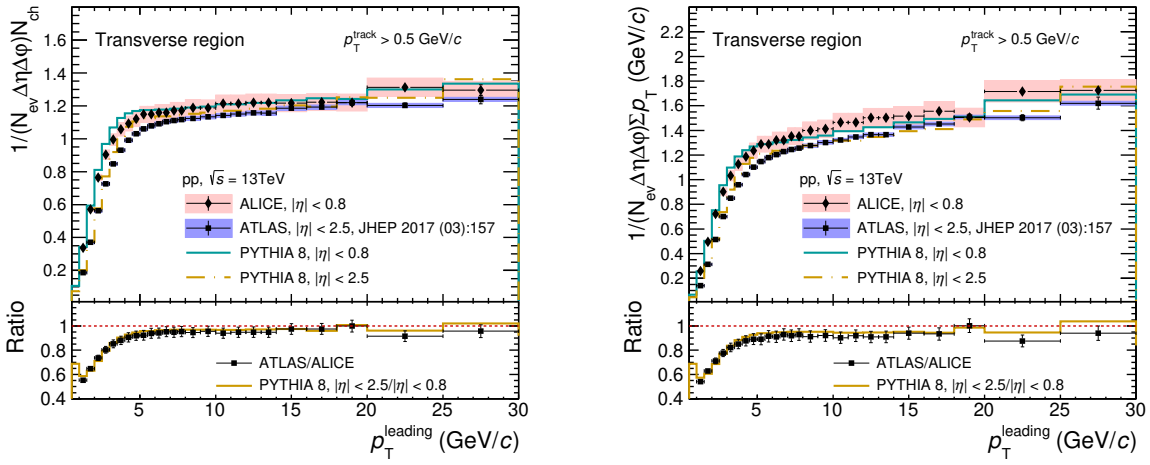

Figure 8. Number density N_{ch} (left) and $\sum p_{\mathrm{T}}$ density (right) in the Transverse region for $p_{\mathrm{T}}^{\mathrm{track}} > 0.5$ GeV/c at $\sqrt{s} = 13$ TeV from ALICE ($|\eta| < 0.8$) and ATLAS ($|\eta| < 2.5$) measurements [13]. The results are compared to PYTHIA 8 Monash-2013 calculations. The shaded areas represent the systematic uncertainties and vertical error bars indicate statistical uncertainties for the data. No uncertainties are shown for the MC simulations.

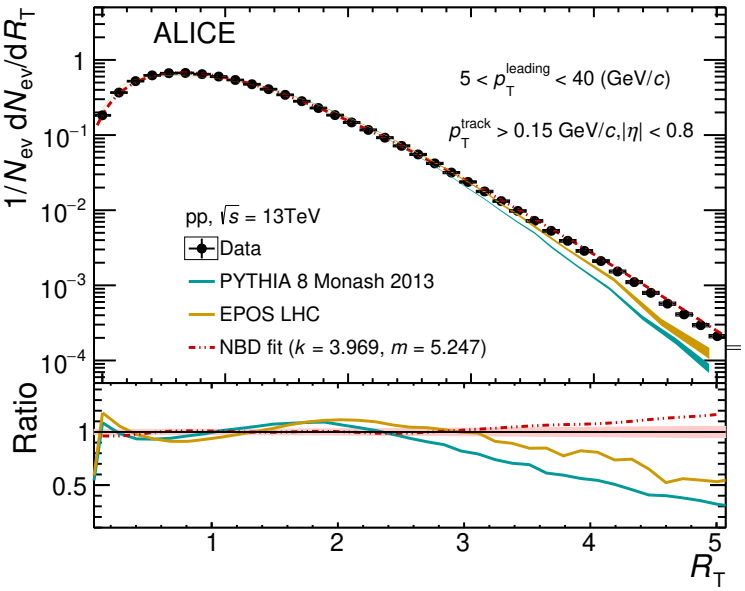

Figure 9. R_{T} probability distribution in the Transverse region for $p_{\mathrm{T}}^{\mathrm{track}} > 0.15$ GeV/c and $|\eta| < 0.8$. The result (solid circles) is compared to the PYTHIA 8 and EPOS LHC calculations (lines). The red line represents the result of the NBD fit, where the multiplicity is scaled by its mean value, m. The parameter k is related to the standard deviation of the distribution via $\sigma = \sqrt{\frac{1}{m} + \frac{1}{k}}$. The open boxes represent the systematic uncertainties and vertical error bars indicate statistical uncertainties for the data. The bands indicate the statistical uncertainties of the MC simulations. The bottom panel shows the ratio between the NBD fit, as well as those of the MC to the data.

JHEP04(2020)192

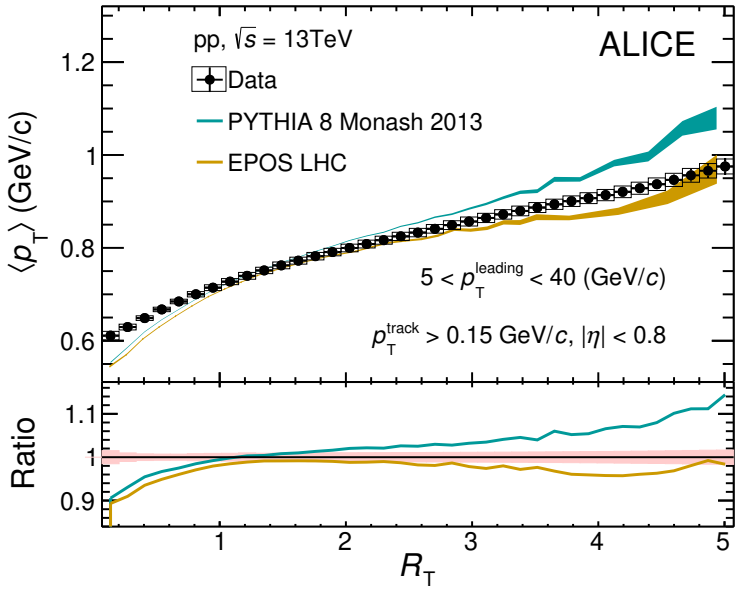

Figure 10. $\langle p_{\mathrm{T}} \rangle$ in the Transverse region as a function of R_{T} for $p_{\mathrm{T}}^{\mathrm{track}} > 0.15$ GeV/c and $|\eta| < 0.8$. Data (solid circles) are compared to the results of PYTHIA 8 and Epos LHC calculations (lines). The open boxes represent the systematic uncertainties and vertical error bars indicate statistical uncertainties for the data. The bands indicate the statistical uncertainties of the MC simulations. The bottom panel shows the ratio of the MC to data.

The charged-particle $\langle p_{\mathrm{T}} \rangle$ distribution as a function of R_{T} is shown in figure 10. The average transverse momentum rises steadily from $\sim$ 0.6 GeV/c at low UE multiplicity to $\sim$ 1 GeV/c for 5 times the mean multiplicity. The results are also compared with the PYTHIA 8 and Epos LHC calculations. While the shapes are similar, both models deviate from the measurement by up to 10%, in particular at the extremes of the R_{T} interval covered by the measurement. Interestingly, at high multiplicity the deviations have opposite signs for the two models, with PYTHIA 8 predicting slightly harder and Epos LHC softer transverse activity than seen in data.

7 Conclusions

The UE properties in pp collisions at $\sqrt{s} = 13$ TeV have been characterized by measuring the number density N_{ch} and $\sum p_{\mathrm{T}}$ density distributions of charged particles in three azimuthal regions with respect to the leading charged-particle direction: Toward, Transverse, and Away. The measurement is performed using charged particles, which have been corrected to the level of primary charged particles. The results are compared to previous ALICE measurements in pp collisions at $\sqrt{s} = 0.9$ and 7 TeV. In this work, the kinematic range of the leading particle is extended, and the uncertainties are reduced. An increase of approximately 30% of the jet pedestal is observed when the pp collision energy increases from $\sqrt{s} = 7$ to 13 TeV. The UE activity, quantified by the charged-particle density in the jet pedestal range in the Transverse region, shows a stronger increase with $\sqrt{s}$ than the inclusive midrapidity charged-particle density in MB events. This is in qualitative agree-

JHEP04(2020)192

ment with an increased relative contribution of hard processes to the UE with increasing $\sqrt{s}$.

The Transverse region has been further characterized by the relative transverse UE activity classifier R_{T}. Measuring UE quantities versus R_{T} yields sensitivity to rare events with exceptionally large or small transverse activity with respect to the event-averaged mean. The models considered in the paper, PYTHIA 8 and EPOS LHC, cannot describe the R_{T} distribution in the full range covered by the measurements ($0 < R_{\mathrm{T}} < 5$). Moreover, whereas the overall agreement with $\langle p_{\mathrm{T}} \rangle$ measured in the transverse region as a function of R_{T} is within 10%, PYTHIA 8 and EPOS LHC show significant deviations at very low and high R_{T}. Compared to data and to each other, these models show a significantly different behavior at high R_{T}. This might be a consequence of how each model treats the high-density events. Therefore, the measurements presented here provide new constraints on the models, particularly to their description of MPI.

Acknowledgments

The ALICE Collaboration would like to thank all its engineers and technicians for their invaluable contributions to the construction of the experiment and the CERN accelerator teams for the outstanding performance of the LHC complex. The ALICE Collaboration gratefully acknowledges the resources and support provided by all Grid centres and the Worldwide LHC Computing Grid (WLCG) collaboration. The ALICE Collaboration acknowledges the following funding agencies for their support in building and running the ALICE detector: A. I. Alikhanyan National Science Laboratory (Yerevan Physics Institute) Foundation (ANSL), State Committee of Science and World Federation of Scientists (WFS), Armenia; Austrian Academy of Sciences, Austrian Science Fund (FWF): [M 2467-N36] and Nationalstiftung für Forschung, Technologie und Entwicklung, Austria; Ministry of Communications and High Technologies, National Nuclear Research Center, Azerbaijan; Conselho Nacional de Desenvolvimento Científico e Tecnológico (CNPq), Financiadora de Estudos e Projetos (Finep), Fundação de Amparo à Pesquisa do Estado de São Paulo (FAPESP) and Universidade Federal do Rio Grande do Sul (UFRGS), Brazil; Ministry of Education of China (MOEC) , Ministry of Science & Technology of China (MSTC) and National Natural Science Foundation of China (NSFC), China; Ministry of Science and Education and Croatian Science Foundation, Croatia; Centro de Aplicaciones Tecnológicas y Desarrollo Nuclear (CEADEN), Cubaenergía, Cuba; Ministry of Education, Youth and Sports of the Czech Republic, Czech Republic; The Danish Council for Independent Research — Natural Sciences, the VILLUM FONDEN and Danish National Research Foundation (DNRF), Denmark; Helsinki Institute of Physics (HIP), Finland; Commissariat à l'Energie Atomique (CEA), Institut National de Physique Nucléaire et de Physique des Particules (IN2P3) and Centre National de la Recherche Scientifique (CNRS) and Région des Pays de la Loire, France; Bundesministerium für Bildung und Forschung (BMBF) and GSI Helmholtzzentrum für Schwerionenforschung GmbH, Germany; General Secretariat for Research and Technology, Ministry of Education, Research and Religions, Greece; National Research, Development and Innovation Office, Hungary; Department of

JHEP04(2020)192

Atomic Energy Government of India (DAE), Department of Science and Technology, Government of India (DST), University Grants Commission, Government of India (UGC) and Council of Scientific and Industrial Research (CSIR), India; Indonesian Institute of Science, Indonesia; Centro Fermi — Museo Storico della Fisica e Centro Studi e Ricerche Enrico Fermi and Istituto Nazionale di Fisica Nucleare (INFN), Italy; Institute for Innovative Science and Technology , Nagasaki Institute of Applied Science (IIST), Japanese Ministry of Education, Culture, Sports, Science and Technology (MEXT) and Japan Society for the Promotion of Science (JSPS) KAKENHI, Japan; Consejo Nacional de Ciencia (CONACYT) y Tecnología, through Fondo de Cooperación Internacional en Ciencia y Tecnología (FONCICYT) and Dirección General de Asuntos del Personal Academico (DGAPA), Mexico; Nederlandse Organisatie voor Wetenschappelijk Onderzoek (NWO), Netherlands; The Research Council of Norway, Norway; Commission on Science and Technology for Sustainable Development in the South (COMSATS), Pakistan; Pontificia Universidad Católica del Perú, Peru; Ministry of Science and Higher Education and National Science Centre, Poland; Korea Institute of Science and Technology Information and National Research Foundation of Korea (NRF), Republic of Korea; Ministry of Education and Scientific Research, Institute of Atomic Physics and Ministry of Research and Innovation and Institute of Atomic Physics, Romania; Joint Institute for Nuclear Research (JINR), Ministry of Education and Science of the Russian Federation, National Research Centre Kurchatov Institute, Russian Science Foundation and Russian Foundation for Basic Research, Russia; Ministry of Education, Science, Research and Sport of the Slovak Republic, Slovakia; National Research Foundation of South Africa, South Africa; Swedish Research Council (VR) and Knut & Alice Wallenberg Foundation (KAW), Sweden; European Organization for Nuclear Research, Switzerland; Suranaree University of Technology (SUT), National Science and Technology Development Agency (NSDTA) and Office of the Higher Education Commission under NRU project of Thailand, Thailand; Turkish Atomic Energy Agency (TAEK), Turkey; National Academy of Sciences of Ukraine, Ukraine; Science and Technology Facilities Council (STFC), United Kingdom; National Science Foundation of the United States of America (NSF) and United States Department of Energy, Office of Nuclear Physics (DOE NP), United States of America.

A Number density N_{ch} and $\sum p_{\mathrm{T}}$ distributions with $p_{\mathrm{T}}^{\mathrm{track}} > 0.5$ and 1.0 GeV/c

The fully corrected distributions of the averaged charged-particle number and summed-p_{T} densities as a function of $p_{\mathrm{T}}^{\mathrm{leading}}$, in the Toward, Transverse, and Away regions for the transverse momentum cuts $p_{\mathrm{T}}^{\mathrm{track}} > 0.5$ and 1.0 GeV/c are presented in figure 11 and 12.

JHEP04(2020)192

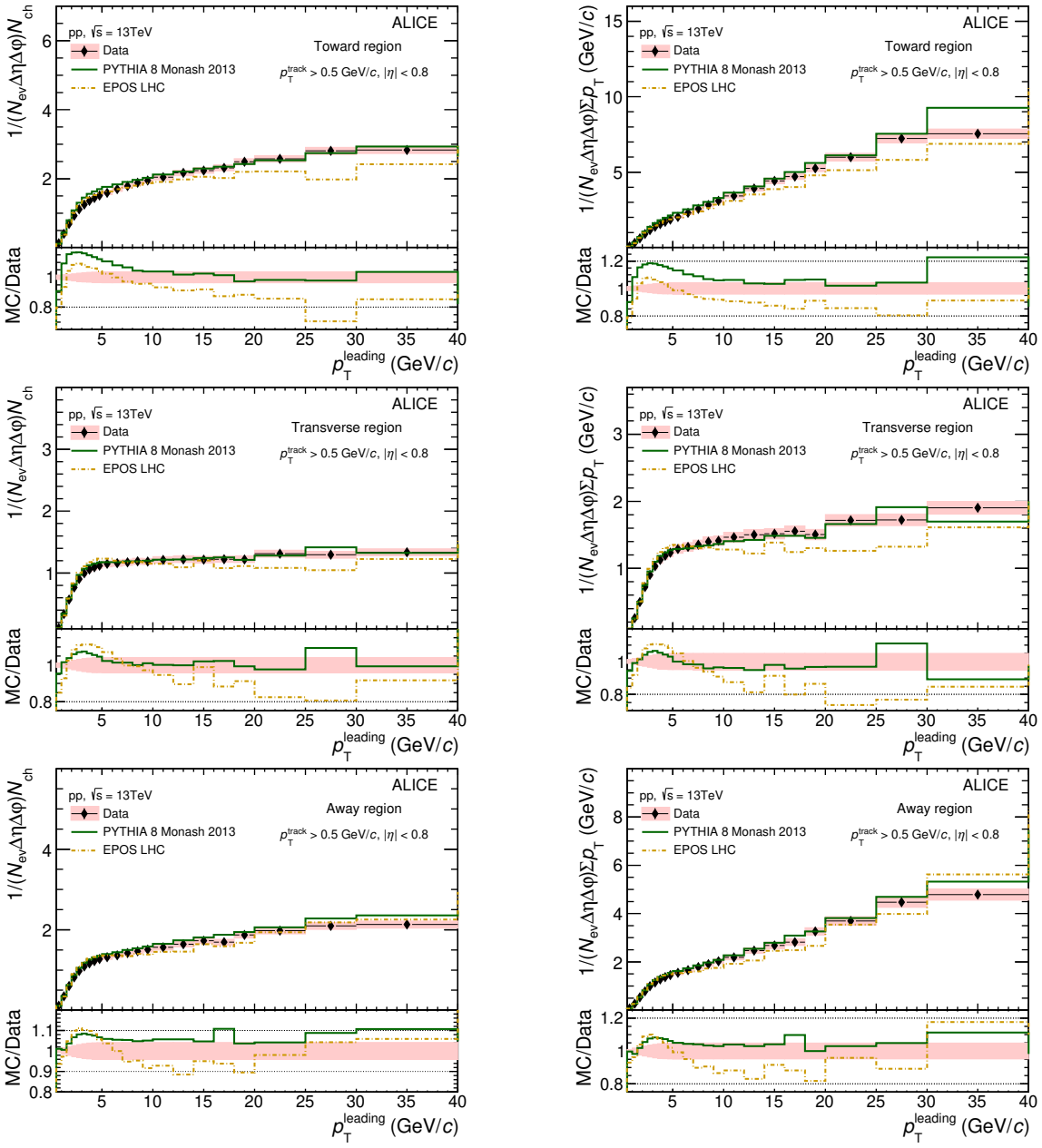

Figure 11. Number density N_{ch} (left) and $\sum p_{\mathrm{T}}$ (right) distributions as a function of $p_{\mathrm{T}}^{\mathrm{leading}}$ compared to MC predictions in Toward (top), Transverse (middle), and Away (bottom) regions for $p_{\mathrm{T}}^{\mathrm{track}} > 0.5$ GeV/c. The shaded areas in the upper panels represent the systematic uncertainties and vertical error bars indicate statistical uncertainties. In the lower panels, the shaded areas are the sum in quadrature of statistical and systematic uncertainties from the upper panels . No uncertainties are given for the MC calculations.

JHEP04(2020)192

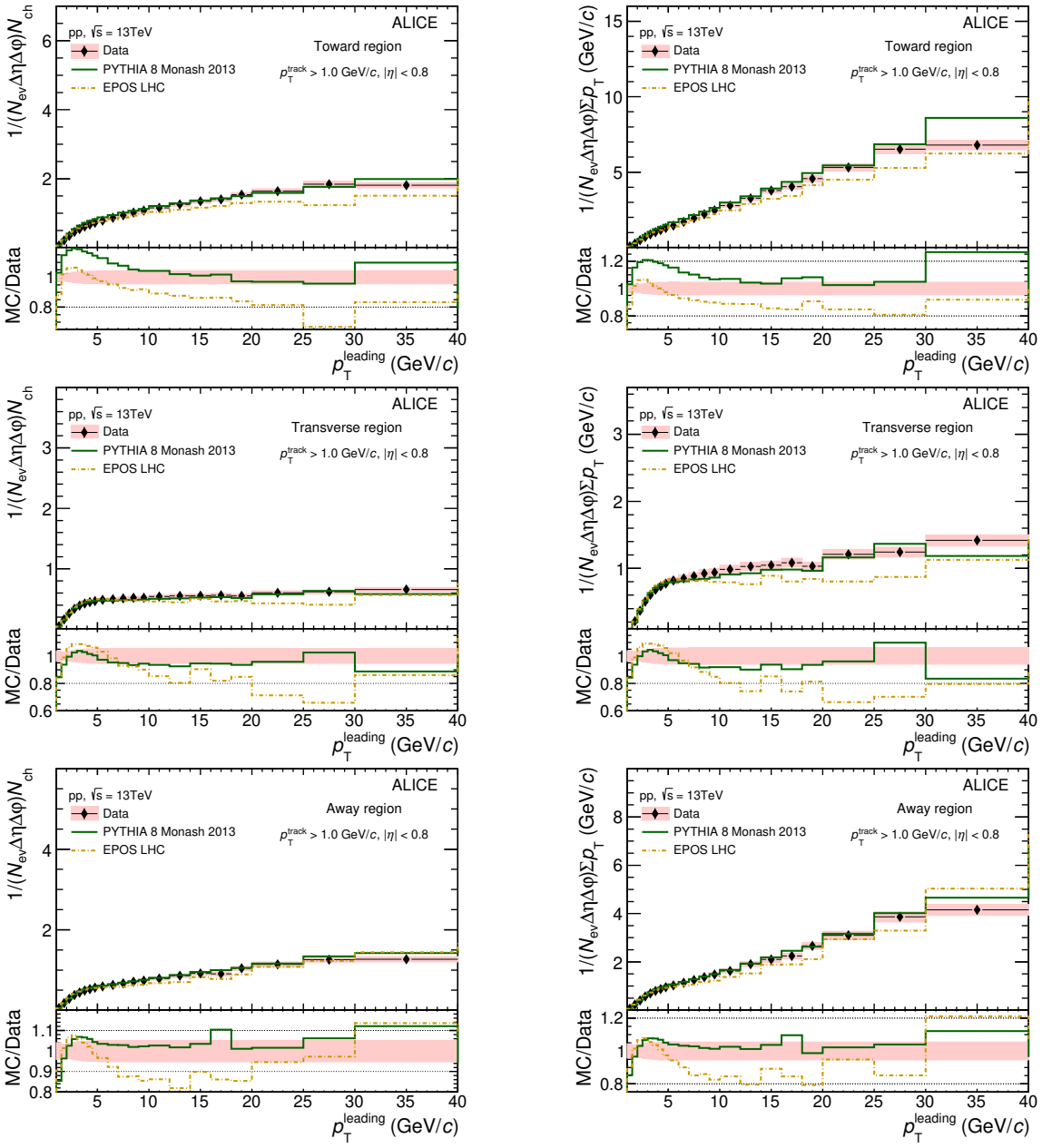

Figure 12. Number density N_{ch} (left) and $\sum p_{\mathrm{T}}$ (right) distributions as a function of $p_{\mathrm{T}}^{\mathrm{leading}}$ and the comparisons to MC predictions in Toward (top), Transverse (middle), and Away (bottom) regions for $p_{\mathrm{T}}^{\mathrm{track}} > 1.0$ GeV/c. The shaded areas in the upper panels represent the systematic uncertainties and vertical error bars indicate statistical uncertainties. In the lower panels, the shaded areas are the sum in quadrature of statistical and systematic uncertainties from the upper panels. No uncertainties are given for the MC calculations.

JHEP04(2020)192

References

[1] P. Bartalini and J.R. Gaunt, *Multiple parton interactions at the LHC*, *Adv. Ser. Direct. High Energy Phys.* **29** (2018) 1 [INSPIRE].

[2] UA1 collaboration, *Hadronic jet production at the CERN proton-anti-proton collider*, *Phys. Lett.* **B 132** (1983) 214 [INSPIRE].

[3] UA1 collaboration, *Production of low transverse energy clusters in $\bar{p}p$ collisions at $\sqrt{s} = 0.2$ TeV to 0.9 TeV and their interpretation in terms of QCD jets*, *Nucl. Phys.* **B 309** (1988) 405 [INSPIRE].

[4] UA1 collaboration, *A study of the general characteristics of $p\bar{p}$ collisions at $\sqrt{s} = 0.2$ TeV to 0.9 TeV*, *Nucl. Phys.* **B 335** (1990) 261 [INSPIRE].

[5] CDF collaboration, *Charged jet evolution and the underlying event in $p\bar{p}$ collisions at 1.8 TeV*, *Phys. Rev.* **D 65** (2002) 092002 [INSPIRE].

[6] CDF collaboration, *The underlying event in hard interactions at the Tevatron $\bar{p}p$ collider*, *Phys. Rev.* **D 70** (2004) 072002 [hep-ex/0404004] [INSPIRE].

[7] R. Field, *Min-bias and the underlying event at the LHC*, *Acta Phys. Polon.* **B 42** (2011) 2631 [arXiv:1110.5530] [INSPIRE].

[8] CDF collaboration, *Studying the underlying event in Drell-Yan and high transverse momentum jet production at the Tevatron*, *Phys. Rev.* **D 82** (2010) 034001 [arXiv:1003.3146] [INSPIRE].

[9] CMS collaboration, *First measurement of the underlying event activity at the LHC with $\sqrt{s} = 0.9$ TeV*, *Eur. Phys. J.* **C 70** (2010) 555 [arXiv:1006.2083] [INSPIRE].

[10] ATLAS collaboration, *Measurement of underlying event characteristics using charged particles in pp collisions at $\sqrt{s} = 900$ GeV and 7 TeV with the ATLAS detector*, *Phys. Rev.* **D 83** (2011) 112001 [arXiv:1012.0791] [INSPIRE].

[11] ALICE collaboration, *Underlying event measurements in pp collisions at $\sqrt{s} = 0.9$ and 7 TeV with the ALICE experiment at the LHC*, *JHEP* **07** (2012) 116 [arXiv:1112.2082] [INSPIRE].

[12] ATLAS collaboration, *Measurement of the underlying event in jet events from 7 TeV proton-proton collisions with the ATLAS detector*, *Eur. Phys. J.* **C 74** (2014) 2965 [arXiv:1406.0392] [INSPIRE].

[13] ATLAS collaboration, *Measurement of charged-particle distributions sensitive to the underlying event in $\sqrt{s} = 13$ TeV proton-proton collisions with the ATLAS detector at the LHC*, *JHEP* **03** (2017) 157 [arXiv:1701.05390] [INSPIRE].

[14] CMS collaboration, *Measurement of the underlying event in the Drell-Yan process in proton-proton collisions at $\sqrt{s} = 7$ TeV*, *Eur. Phys. J.* **C 72** (2012) 2080 [arXiv:1204.1411] [INSPIRE].

[15] ATLAS collaboration, *Measurement of distributions sensitive to the underlying event in inclusive Z-boson production in pp collisions at $\sqrt{s} = 7$ TeV with the ATLAS detector*, *Eur. Phys. J.* **C 74** (2014) 3195 [arXiv:1409.3433] [INSPIRE].

JHEP04(2020)192

[16] CMS collaboration, *Measurement of the underlying event activity in inclusive Z boson production in proton-proton collisions at* $\sqrt{s} = 13$ *TeV*, *JHEP* **07** (2018) 032 [arXiv:1711.04299] [INSPIRE].

[17] ATLAS collaboration, *Measurement of distributions sensitive to the underlying event in inclusive Z-boson production in pp collisions at* $\sqrt{s} = 13$ *TeV with the ATLAS detector*, *Eur. Phys. J.* **C 79** (2019) 666 [arXiv:1905.09752] [INSPIRE].

[18] T. Sjöstrand and M. van Zijl, *A multiple interaction model for the event structure in hadron collisions*, *Phys. Rev.* **D 36** (1987) 2019 [INSPIRE].

[19] T. Sjöstrand and P.Z. Skands, *Multiple interactions and the structure of beam remnants*, *JHEP* **03** (2004) 053 [hep-ph/0402078] [INSPIRE].

[20] T. Sjöstrand and P.Z. Skands, *Transverse-momentum-ordered showers and interleaved multiple interactions*, *Eur. Phys. J.* **C 39** (2005) 129 [hep-ph/0408302] [INSPIRE].

[21] CMS collaboration, *Event generator tunes obtained from underlying event and multiparton scattering measurements*, *Eur. Phys. J.* **C 76** (2016) 155 [arXiv:1512.00815] [INSPIRE].

[22] ALICE collaboration, *Centrality dependence of particle production in p-Pb collisions at* $\sqrt{s_{\rm NN}} = 5.02$ *TeV*, *Phys. Rev.* **C 91** (2015) 064905 [arXiv:1412.6828] [INSPIRE].

[23] C. Loizides and A. Morsch, *Absence of jet quenching in peripheral nucleus-nucleus collisions*, *Phys. Lett.* **B 773** (2017) 408 [arXiv:1705.08856] [INSPIRE].

[24] ALICE collaboration, *Analysis of the apparent nuclear modification in peripheral Pb-Pb collisions at* 5.02 *TeV*, *Phys. Lett.* **B 793** (2019) 420 [arXiv:1805.05212] [INSPIRE].

[25] J.L. Nagle and W.A. Zajc, *Small system collectivity in relativistic hadronic and nuclear collisions*, *Ann. Rev. Nucl. Part. Sci.* **68** (2018) 211 [arXiv:1801.03477] [INSPIRE].

[26] E. Norbeck, K. Šafařík and P.A. Steinberg, *Hard-scattering results in heavy-ion collisions at the LHC*, *Ann. Rev. Nucl. Part. Sci.* **64** (2014) 383 [INSPIRE].

[27] N. Armesto and E. Scomparin, *Heavy-ion collisions at the Large Hadron Collider: a review of the results from run* 1, *Eur. Phys. J. Plus* **131** (2016) 52 [arXiv:1511.02151] [INSPIRE].

[28] B.G. Zakharov, *Jet quenching in pp and pA collisions*, *AIP Conf. Proc.* **1701** (2016) 060001 [arXiv:1412.0295] [INSPIRE].

[29] T. Martin, P. Skands and S. Farrington, *Probing collective effects in hadronisation with the extremes of the underlying event*, *Eur. Phys. J.* **C 76** (2016) 299 [arXiv:1603.05298] [INSPIRE].

[30] S.G. Weber, A. Dubla, A. Andronic and A. Morsch, *Elucidating the multiplicity dependence of* J/ψ *production in proton-proton collisions with PYTHIA*8, *Eur. Phys. J.* **C 79** (2019) 36 [arXiv:1811.07744] [INSPIRE].

[31] ALICE collaboration, *The ALICE definition of primary particles*, ALICE-PUBLIC-2017-005, CERN, Geneva, Switzerland (2018), pg. 1.

[32] T. Sjöstrand, S. Mrenna and P.Z. Skands, *A brief introduction to PYTHIA* 8.1, *Comput. Phys. Commun.* **178** (2008) 852 [arXiv:0710.3820] [INSPIRE].

[33] H.J. Drescher, M. Hladik, S. Ostapchenko, T. Pierog and K. Werner, *Parton based Gribov-Regge theory*, *Phys. Rept.* **350** (2001) 93 [hep-ph/0007198] [INSPIRE].

[34] Particle Data Group collaboration, *Review of particle physics*, *Phys. Rev.* **D 98** (2018) 030001 [INSPIRE].

[35] B. Andersson, G. Gustafson, G. Ingelman and T. Sjöstrand, *Parton fragmentation and string dynamics*, *Phys. Rept.* **97** (1983) 31 [INSPIRE].

[36] T. Sjöstrand, S. Mrenna and P.Z. Skands, *PYTHIA* 6.4 *physics and manual*, *JHEP* **05** (2006) 026 [hep-ph/0603175] [INSPIRE].

JHEP04(2020)192

[37] P. Skands, S. Carrazza and J. Rojo, *Tuning PYTHIA* 8.1*: the Monash* 2013 *tune*, *Eur. Phys. J.* **C 74** (2014) 3024 [arXiv:1404.5630] [INSPIRE].

[38] NNPDF collaboration, *Parton distributions with QED corrections*, *Nucl. Phys.* **B 877** (2013) 290 [arXiv:1308.0598] [INSPIRE].

[39] K. Werner, F.-M. Liu and T. Pierog, *Parton ladder splitting and the rapidity dependence of transverse momentum spectra in deuteron-gold collisions at RHIC*, *Phys. Rev.* **C 74** (2006) 044902 [hep-ph/0506232] [INSPIRE].

[40] T. Pierog, I. Karpenko, J.M. Katzy, E. Yatsenko and K. Werner, *EPOS LHC: test of collective hadronization with data measured at the CERN Large Hadron Collider*, *Phys. Rev.* **C 92** (2015) 034906 [arXiv:1306.0121] [INSPIRE].

[41] ALICE collaboration, *The ALICE experiment at the CERN LHC*, 2008 *JINST* **3** S08002 [INSPIRE].

[42] ALICE collaboration, *Performance of the ALICE experiment at the CERN LHC*, *Int. J. Mod. Phys.* **A 29** (2014) 1430044 [arXiv:1402.4476] [INSPIRE].

[43] P. Skands, S. Carrazza and J. Rojo, *Tuning PYTHIA* 8.1*: the Monash* 2013 *tune*, *Eur. Phys. J.* **C 74** (2014) 3024 [arXiv:1404.5630] [INSPIRE].

[44] R. Brun et al., *GEANT: detector description and simulation tool*, CERN-W-5013, CERN, Geneva, Switzerland (1994), pg. 1.

[45] ALICE collaboration, *Transverse momentum spectra of charged particles in proton-proton collisions at* $\sqrt{s} = 900$ *GeV with ALICE at the LHC*, *Phys. Lett.* **B 693** (2010) 53 [arXiv:1007.0719] [INSPIRE].

[46] ALICE collaboration, *Multiplicity dependence of the average transverse momentum in pp, p-Pb and Pb-Pb collisions at the LHC*, *Phys. Lett.* **B 727** (2013) 371 [arXiv:1307.1094] [INSPIRE].

[47] G. D'Agostini, *A multidimensional unfolding method based on Bayes' theorem*, *Nucl. Instrum. Meth.* **A 362** (1995) 487 [INSPIRE].

[48] T. Adye, *Unfolding algorithms and tests using RooUnfold*, in *Proceedings, PHYSTAT* 2011 *Workshop on Statistical Issues Related to Discovery Claims in Search Experiments and Unfolding*, CERN, Geneva, Switzerland, 17–20 January 2011, pg. 313 [arXiv:1105.1160] [INSPIRE].

[49] A. Hocker and V. Kartvelishvili, *SVD approach to data unfolding*, *Nucl. Instrum. Meth.* **A 372** (1996) 469 [hep-ph/9509307] [INSPIRE].

[50] ALICE collaboration, *Energy dependence of the transverse momentum distributions of charged particles in pp collisions measured by ALICE*, *Eur. Phys. J.* **C 73** (2013) 2662 [arXiv:1307.1093] [INSPIRE].

[51] ALICE collaboration, *Pseudorapidity and transverse-momentum distributions of charged particles in proton-proton collisions at* $\sqrt{s} = 13$ *TeV*, *Phys. Lett.* **B 753** (2016) 319 [arXiv:1509.08734] [INSPIRE].

[52] K. Werner, B. Guiot, I. Karpenko and T. Pierog, *New developments in EPOS: parton saturation*, *J. Phys. Conf. Ser.* **458** (2013) 012020 [INSPIRE].

[53] T. Pierog, B. Guiot, I. Karpenko, G. Sophys, M. Stefaniak and K. Werner, *EPOS* 3 *and air showers*, *EPJ Web Conf.* **210** (2019) 02008 [INSPIRE].

[54] ATLAS collaboration, *Charged-particle distributions in* $\sqrt{s} = 13$ *TeV pp interactions measured with the ATLAS detector at the LHC*, *Phys. Lett.* **B 758** (2016) 67 [arXiv:1602.01633] [INSPIRE].

JHEP04(2020)192

The ALICE collaboration

S. Acharya[141], D. Adamová[94], A. Adler[74], J. Adolfsson[80], M.M. Aggarwal[99], G. Aglieri Rinella[33], M. Agnello[30], N. Agrawal[10,53], Z. Ahammed[141], S. Ahmad[16], S.U. Ahn[76], A. Akindinov[91], M. Al-Turany[106], S.N. Alam[141], D.S.D. Albuquerque[122], D. Aleksandrov[87], B. Alessandro[58], H.M. Alfanda[6], R. Alfaro Molina[71], B. Ali[16], Y. Ali[14], A. Alici[10,26,53], A. Alkin[2], J. Alme[21], T. Alt[68], L. Altenkamper[21], I. Altsybeev[112], M.N. Anaam[6], C. Andrei[47], D. Andreou[33], H.A. Andrews[110], A. Andronic[144], M. Angeletti[33], V. Anguelov[103], C. Anson[15], T. Antičić[107], F. Antinori[56], P. Antonioli[53], R. Anwar[125], N. Apadula[79], L. Aphecetche[114], H. Appelshäuser[68], S. Arcelli[26], R. Arnaldi[58], M. Arratia[79], I.C. Arsene[20], M. Arslandok[103], A. Augustinus[33], R. Averbeck[106], S. Aziz[61], M.D. Azmi[16], A. Badalà[55], Y.W. Baek[40], S. Bagnasco[58], X. Bai[106], R. Bailhache[68], R. Bala[100], A. Baldisseri[137], M. Ball[42], S. Balouza[104], R. Barbera[27], L. Barioglio[25], G.G. Barnaföldi[145], L.S. Barnby[93], V. Barret[134], P. Bartalini[6], K. Barth[33], E. Bartsch[68], F. Baruffaldi[28], N. Bastid[134], S. Basu[143], G. Batigne[114], B. Batyunya[75], D. Bauri[48], J.L. Bazo Alba[111], I.G. Bearden[88], C. Bedda[63], N.K. Behera[60], I. Belikov[136], A.D.C. Bell Hechavarria[144], F. Bellini[33], R. Bellwied[125], V. Belyaev[92], G. Bencedi[145], S. Beole[25], A. Bercuci[47], Y. Berdnikov[97], D. Berenyi[145], R.A. Bertens[130], D. Berzano[58], M.G. Besoiu[67], L. Betev[33], A. Bhasin[100], I.R. Bhat[100], M.A. Bhat[3], H. Bhatt[48], B. Bhattacharjee[41], A. Bianchi[25], L. Bianchi[25], N. Bianchi[51], J. Bielčík[36], J. Bielčíková[94], A. Bilandzic[104,117], G. Biro[145], R. Biswas[3], S. Biswas[3], J.T. Blair[119], D. Blau[87], C. Blume[68], G. Boca[139], F. Bock[33,95], A. Bogdanov[92], S. Boi[23], L. Boldizsár[145], A. Bolozdynya[92], M. Bombara[37], G. Bonomi[140], H. Borel[137], A. Borissov[92,144], H. Bossi[146], E. Botta[25], L. Bratrud[68], P. Braun-Munzinger[106], M. Bregant[121], M. Broz[36], E.J. Brucken[43], E. Bruna[58], G.E. Bruno[105], M.D. Buckland[127], D. Budnikov[108], H. Buesching[68], S. Bufalino[30], O. Bugnon[114], P. Buhler[113], P. Buncic[33], Z. Buthelezi[72,131], J.B. Butt[14], J.T. Buxton[96], S.A. Bysiak[118], D. Caffarri[89], A. Caliva[106], E. Calvo Villar[111], R.S. Camacho[44], P. Camerini[24], A.A. Capon[113], F. Carnesecchi[10,26], R. Caron[137], J. Castillo Castellanos[137], A.J. Castro[130], E.A.R. Casula[54], F. Catalano[30], C. Ceballos Sanchez[52], P. Chakraborty[48], S. Chandra[141], W. Chang[6], S. Chapeland[33], M. Chartier[127], S. Chattopadhyay[141], S. Chattopadhyay[109], A. Chauvin[23], C. Cheshkov[135], B. Cheynis[135], V. Chibante Barroso[33], D.D. Chinellato[122], S. Cho[60], P. Chochula[33], T. Chowdhury[134], P. Christakoglou[89], C.H. Christensen[88], P. Christiansen[80], T. Chujo[133], C. Cicalo[54], L. Cifarelli[10,26], F. Cindolo[53], J. Cleymans[124], F. Colamaria[52], D. Colella[52], A. Collu[79], M. Colocci[26], M. Concas[58, ii], G. Conesa Balbastre[78], Z. Conesa del Valle[61], G. Contin[24,127], J.G. Contreras[36], T.M. Cormier[95], Y. Corrales Morales[25], P. Cortese[31], M.R. Cosentino[123], F. Costa[33], S. Costanza[139], P. Crochet[134], E. Cuautle[69], P. Cui[6], L. Cunqueiro[95], D. Dabrowski[142], T. Dahms[104,117], A. Dainese[56], F.P.A. Damas[114,137], M.C. Danisch[103], A. Danu[67], D. Das[109], I. Das[109], P. Das[85], P. Das[3], S. Das[3], A. Dash[85], S. Dash[48], S. De[85], A. De Caro[29], G. de Cataldo[52], J. de Cuveland[38], A. De Falco[23], D. De Gruttola[10], N. De Marco[58], S. De Pasquale[29], S. Deb[49], B. Debjani[3], H.F. Degenhardt[121], K.R. Deja[142], A. Deloff[84], S. Delsanto[25,131], D. Devetak[106], P. Dhankher[48], D. Di Bari[32], A. Di Mauro[33], R.A. Diaz[8], T. Dietel[124], P. Dillenseger[68], Y. Ding[6], R. Divià[33], D.U. Dixit[19], Ø. Djuvsland[21], U. Dmitrieva[62], A. Dobrin[33,67], B. Dönigus[68], O. Dordic[20], A.K. Dubey[141], A. Dubla[106], S. Dudi[99], M. Dukhishyam[85], P. Dupieux[134], R.J. Ehlers[146], V.N. Eikeland[21], D. Elia[52], H. Engel[74], E. Epple[146], B. Erazmus[114], F. Erhardt[98], A. Erokhin[112], M.R. Ersdal[21], B. Espagnon[61], G. Eulisse[33], D. Evans[110], S. Evdokimov[90], L. Fabbietti[104,117], M. Faggin[28], J. Faivre[78], F. Fan[6], A. Fantoni[51], M. Fasel[95], P. Fecchio[30], A. Feliciello[58], G. Feofilov[112], A. Fernández Téllez[44], A. Ferrero[137], A. Ferretti[25], A. Festanti[33], V.J.G. Feuillard[103], J. Figiel[118], S. Filchagin[108], D. Finogeev[62], F.M. Fionda[21], G. Fiorenza[52], F. Flor[125], S. Foertsch[72],

JHEP04(2020)192

P. Foka[106], S. Fokin[87], E. Fragiacomo[59], U. Frankenfeld[106], U. Fuchs[33], C. Furget[78], A. Furs[62], M. Fusco Girard[29], J.J. Gaardhøje[88], M. Gagliardi[25], A.M. Gago[111], A. Gal[136], C.D. Galvan[120], P. Ganoti[83], C. Garabatos[106], E. Garcia-Solis[11], K. Garg[27], C. Gargiulo[33], A. Garibli[86], K. Garner[144], P. Gasik[104,117], E.F. Gauger[119], M.B. Gay Ducati[70], M. Germain[114], J. Ghosh[109], P. Ghosh[141], S.K. Ghosh[3], P. Gianotti[51], P. Giubellino[58,106], P. Giubilato[28], P. Glässel[103], D.M. Goméz Coral[71], A. Gomez Ramirez[74], V. Gonzalez[106], P. González-Zamora[44], S. Gorbunov[38], L. Görlich[118], S. Gotovac[34], V. Grabski[71], L.K. Graczykowski[142], K.L. Graham[110], L. Greiner[79], A. Grelli[63], C. Grigoras[33], V. Grigoriev[92], A. Grigoryan[1], S. Grigoryan[75], O.S. Groettvik[21], F. Grosa[30], J.F. Grosse-Oetringhaus[33], R. Grosso[106], R. Guernane[78], M. Guittiere[114], K. Gulbrandsen[88], T. Gunji[132], A. Gupta[100], R. Gupta[100], I.B. Guzman[44], R. Haake[146], M.K. Habib[106], C. Hadjidakis[61], H. Hamagaki[81], G. Hamar[145], M. Hamid[6], R. Hannigan[119], M.R. Haque[63,85], A. Harlenderova[106], J.W. Harris[146], A. Harton[11], J.A. Hasenbichler[33], H. Hassan[95], D. Hatzifotiadou[10,53], P. Hauer[42], S. Hayashi[132], S.T. Heckel[68,104], E. Hellbär[68], H. Helstrup[35], A. Herghelegiu[47], T. Herman[36], E.G. Hernandez[44], G. Herrera Corral[9], F. Herrmann[144], K.F. Hetland[35], T.E. Hilden[43], H. Hillemanns[33], C. Hills[127], B. Hippolyte[136], B. Hohlweger[104], D. Horak[36], A. Hornung[68], S. Hornung[106], R. Hosokawa[15,133], P. Hristov[33], C. Huang[61], C. Hughes[130], P. Huhn[68], T.J. Humanic[96], H. Hushnud[109], L.A. Husova[144], N. Hussain[41], S.A. Hussain[14], D. Hutter[38], J.P. Iddon[33,127], R. Ilkaev[108], M. Inaba[133], G.M. Innocenti[33], M. Ippolitov[87], A. Isakov[94], M.S. Islam[109], M. Ivanov[106], V. Ivanov[97], V. Izucheev[90], B. Jacak[79], N. Jacazio[53], P.M. Jacobs[79], S. Jadlovska[116], J. Jadlovsky[116], S. Jaelani[63], C. Jahnke[121], M.J. Jakubowska[142], M.A. Janik[142], T. Janson[74], M. Jercic[98], O. Jevons[110], M. Jin[125], F. Jonas[95,144], P.G. Jones[110], J. Jung[68], M. Jung[68], A. Jusko[110], P. Kalinak[64], A. Kalweit[33], V. Kaplin[92], S. Kar[6], A. Karasu Uysal[77], O. Karavichev[62], T. Karavicheva[62], P. Karczmarczyk[33], E. Karpechev[62], A. Kazantsev[87], U. Kebschull[74], R. Keidel[46], M. Keil[33], B. Ketzer[42], Z. Khabanova[89], A.M. Khan[6], S. Khan[16], S.A. Khan[141], A. Khanzadeev[97], Y. Kharlov[90], A. Khatun[16], A. Khuntia[118], B. Kileng[35], B. Kim[60], B. Kim[133], D. Kim[147], D.J. Kim[126], E.J. Kim[73], H. Kim[17,147], J. Kim[147], J.S. Kim[40], J. Kim[103], J. Kim[147], J. Kim[73], M. Kim[103], S. Kim[18], T. Kim[147], T. Kim[147], S. Kirsch[38,68], I. Kisel[38], S. Kiselev[91], A. Kisiel[142], J.L. Klay[5], C. Klein[68], J. Klein[58], S. Klein[79], C. Klein-Bösing[144], M. Kleiner[68], A. Kluge[33], M.L. Knichel[33], A.G. Knospe[125], C. Kobdaj[115], M.K. Köhler[103], T. Kollegger[106], A. Kondratyev[75], N. Kondratyeva[92], E. Kondratyuk[90], J. Konig[68], P.J. Konopka[33], L. Koska[116], O. Kovalenko[84], V. Kovalenko[112], M. Kowalski[118], I. Králik[64], A. Kravčáková[37], L. Kreis[106], M. Krivda[64,110], F. Krizek[94], K. Krizkova Gajdosova[36], M. Krüger[68], E. Kryshen[97], M. Krzewicki[38], A.M. Kubera[96], V. Kučera[60], C. Kuhn[136], P.G. Kuijer[89], L. Kumar[99], S. Kumar[48], S. Kundu[85], P. Kurashvili[84], A. Kurepin[62], A.B. Kurepin[62], A. Kuryakin[108], S. Kushpil[94], J. Kvapil[110], M.J. Kweon[60], J.Y. Kwon[60], Y. Kwon[147], S.L. La Pointe[38], P. La Rocca[27], Y.S. Lai[79], R. Langoy[129], K. Lapidus[33], A. Lardeux[20], P. Larionov[51], E. Laudi[33], R. Lavicka[36], T. Lazareva[112], R. Lea[24], L. Leardini[103], J. Lee[133], S. Lee[147], F. Lehas[89], S. Lehner[113], J. Lehrbach[38], R.C. Lemmon[93], I. León Monzón[120], E.D. Lesser[19], M. Lettrich[33], P. Lévai[145], X. Li[12], X.L. Li[6], J. Lien[129], R. Lietava[110], B. Lim[17], V. Lindenstruth[38], S.W. Lindsay[127], C. Lippmann[106], M.A. Lisa[96], V. Litichevskyi[43], A. Liu[19], S. Liu[96], W.J. Llope[143], I.M. Lofnes[21], V. Loginov[92], C. Loizides[95], P. Loncar[34], X. Lopez[134], E. López Torres[8], J.R. Luhder[144], M. Lunardon[28], G. Luparello[59], Y. Ma[39], A. Maevskaya[62], M. Mager[33], S.M. Mahmood[20], T. Mahmoud[42], A. Maire[136], R.D. Majka[146], M. Malaev[97], Q.W. Malik[20], L. Malinina[75,iii], D. Mal'Kevich[91], P. Malzacher[106], G. Mandaglio[55], V. Manko[87], F. Manso[134], V. Manzari[52], Y. Mao[6], M. Marchisone[135], J. Mareš[66], G.V. Margagliotti[24], A. Margotti[53], J. Margutti[63], A. Marín[106], C. Markert[119], M. Marquard[68], N.A. Martin[103], P. Martinengo[33], J.L. Martinez[125], M.I. Martínez[44], G. Martínez García[114], M. Martinez

JHEP04(2020)192

Pedreira[33], S. Masciocchi[106], M. Masera[25], A. Masoni[54], L. Massacrier[61], E. Masson[114], A. Mastroserio[52,138], A.M. Mathis[104,117], O. Matonoha[80], P.F.T. Matuoka[121], A. Matyja[118], C. Mayer[118], M. Mazzilli[52], M.A. Mazzoni[57], A.F. Mechler[68], F. Meddi[22], Y. Melikyan[62,92], A. Menchaca-Rocha[71], C. Mengke[6], E. Meninno[29,113], M. Meres[13], S. Mhlanga[124], Y. Miake[133], L. Micheletti[25], D.L. Mihaylov[104], K. Mikhaylov[75,91], A. Mischke[63, i], A.N. Mishra[69], D. Miśkowiec[106], A. Modak[3], N. Mohammadi[33], A.P. Mohanty[63], B. Mohanty[85], M. Mohisin Khan[16, iv], C. Mordasini[104], D.A. Moreira De Godoy[144], L.A.P. Moreno[44], I. Morozov[62], A. Morsch[33], T. Mrnjavac[33], V. Muccifora[51], E. Mudnic[34], D. Mühlheim[144], S. Muhuri[141], J.D. Mulligan[79], M.G. Munhoz[121], R.H. Munzer[68], H. Murakami[132], S. Murray[124], L. Musa[33], J. Musinsky[64], C.J. Myers[125], J.W. Myrcha[142], B. Naik[48], R. Nair[84], B.K. Nandi[48], R. Nania[10,53], E. Nappi[52], M.U. Naru[14], A.F. Nassirpour[80], C. Nattrass[130], R. Nayak[48], T.K. Nayak[85], S. Nazarenko[108], A. Neagu[20], R.A. Negrao De Oliveira[68], L. Nellen[69], S.V. Nesbo[35], G. Neskovic[38], D. Nesterov[112], L.T. Neumann[142], B.S. Nielsen[88], S. Nikolaev[87], S. Nikulin[87], V. Nikulin[97], F. Noferini[10,53], P. Nomokonov[75], J. Norman[78,127], N. Novitzky[133], P. Nowakowski[142], A. Nyanin[87], J. Nystrand[21], M. Ogino[81], A. Ohlson[80,103], J. Oleniacz[142], A.C. Oliveira Da Silva[121,130], M.H. Oliver[146], C. Oppedisano[58], R. Orava[43], A. Ortiz Velasquez[69], A. Oskarsson[80], J. Otwinowski[118], K. Oyama[81], Y. Pachmayer[103], V. Pacik[88], D. Pagano[140], G. Paić[69], J. Pan[143], A.K. Pandey[48], S. Panebianco[137], P. Pareek[49,141], J. Park[60], J.E. Parkkila[126], S. Parmar[99], S.P. Pathak[125], R.N. Patra[141], B. Paul[23,58], H. Pei[6], T. Peitzmann[63], X. Peng[6], L.G. Pereira[70], H. Pereira Da Costa[137], D. Peresunko[87], G.M. Perez[8], E. Perez Lezama[68], V. Peskov[68], Y. Pestov[4], V. Petráček[36], M. Petrovici[47], R.P. Pezzi[70], S. Piano[59], M. Pikna[13], P. Pillot[114], O. Pinazza[33,53], L. Pinsky[125], C. Pinto[27], S. Pisano[10,51], D. Pistone[55], M. Płoskoń[79], M. Planinic[98], F. Pliquett[68], J. Pluta[142], S. Pochybova[145, i], M.G. Poghosyan[95], B. Polichtchouk[90], N. Poljak[98], A. Pop[47], H. Poppenborg[144], S. Porteboeuf-Houssais[134], V. Pozdniakov[75], S.K. Prasad[3], R. Preghenella[53], F. Prino[58], C.A. Pruneau[143], I. Pshenichnov[62], M. Puccio[25,33], J. Putschke[143], R.E. Quishpe[125], S. Ragoni[110], S. Raha[3], S. Rajput[100], J. Rak[126], A. Rakotozafindrabe[137], L. Ramello[31], F. Rami[136], R. Raniwala[101], S. Raniwala[101], S.S. Räsänen[43], R. Rath[49], V. Ratza[42], I. Ravasenga[30,89], K.F. Read[95,130], K. Redlich[84, v], A. Rehman[21], P. Reichelt[68], F. Reidt[33], X. Ren[6], R. Renfordt[68], Z. Rescakova[37], J.-P. Revol[10], K. Reygers[103], V. Riabov[97], T. Richert[80,88], M. Richter[20], P. Riedler[33], W. Riegler[33], F. Riggi[27], C. Ristea[67], S.P. Rode[49], M. Rodríguez Cahuantzi[44], K. Røed[20], R. Rogalev[90], E. Rogochaya[75], D. Rohr[33], D. Röhrich[21], P.S. Rokita[142], F. Ronchetti[51], E.D. Rosas[69], K. Roslon[142], A. Rossi[28,56], A. Rotondi[139], A. Roy[49], P. Roy[109], O.V. Rueda[80], R. Rui[24], B. Rumyantsev[75], A. Rustamov[86], E. Ryabinkin[87], Y. Ryabov[97], A. Rybicki[118], H. Rytkonen[126], O.A.M. Saarimaki[43], S. Sadhu[141], S. Sadovsky[90], K. Šafařík[36], S.K. Saha[141], B. Sahoo[48], P. Sahoo[48,49], R. Sahoo[49], S. Sahoo[65], P.K. Sahu[65], J. Saini[141], S. Sakai[133], S. Sambyal[100], V. Samsonov[92,97], D. Sarkar[143], N. Sarkar[141], P. Sarma[41], V.M. Sarti[104], M.H.P. Sas[63], E. Scapparone[53], B. Schaefer[95], J. Schambach[119], H.S. Scheid[68], C. Schiaua[47], R. Schicker[103], A. Schmah[103], C. Schmidt[106], H.R. Schmidt[102], M.O. Schmidt[103], M. Schmidt[102], N.V. Schmidt[68,95], A.R. Schmier[130], J. Schukraft[88], Y. Schutz[33,136], K. Schwarz[106], K. Schweda[106], G. Scioli[26], E. Scomparin[58], M. Šefčík[37], J.E. Seger[15], Y. Sekiguchi[132], D. Sekihata[132], I. Selyuzhenkov[92,106], S. Senyukov[136], D. Serebryakov[62], E. Serradilla[71], A. Sevcenco[67], A. Shabanov[62], A. Shabetai[114], R. Shahoyan[33], W. Shaikh[109], A. Shangaraev[90], A. Sharma[99], A. Sharma[100], H. Sharma[118], M. Sharma[100], N. Sharma[99], A.I. Sheikh[141], K. Shigaki[45], M. Shimomura[82], S. Shirinkin[91], Q. Shou[39], Y. Sibiriak[87], S. Siddhanta[54], T. Siemiarczuk[84], D. Silvermyr[80], G. Simatovic[89], G. Simonetti[33,104], R. Singh[85], R. Singh[100], R. Singh[49], V.K. Singh[141], V. Singhal[141], T. Sinha[109], B. Sitar[13], M. Sitta[31], T.B. Skaali[20], M. Slupecki[126], N. Smirnov[146], R.J.M. Snellings[63], T.W. Snellman[43,126],

JHEP04(2020)192

C. Soncco[111], J. Song[60,125], A. Songmoolnak[115], F. Soramel[28], S. Sorensen[130], I. Sputowska[118], J. Stachel[103], I. Stan[67], P. Stankus[95], P.J. Steffanic[130], E. Stenlund[80], D. Stocco[114], M.M. Storetvedt[35], L.D. Stritto[29], A.A.P. Suaide[121], T. Sugitate[45], C. Suire[61], M. Suleymanov[14], M. Suljic[33], R. Sultanov[91], M. Šumbera[94], S. Sumowidagdo[50], S. Swain[65], A. Szabo[13], I. Szarka[13], U. Tabassam[14], G. Taillepied[134], J. Takahashi[122], G.J. Tambave[21], S. Tang[6,134], M. Tarhini[114], M.G. Tarzila[47], A. Tauro[33], G. Tejeda Muñoz[44], A. Telesca[33], C. Terrevoli[125], D. Thakur[49], S. Thakur[141], D. Thomas[119], F. Thoresen[88], R. Tieulent[135], A. Tikhonov[62], A.R. Timmins[125], A. Toia[68], N. Topilskaya[62], M. Toppi[51], F. Torales-Acosta[19], S.R. Torres[9,120], A. Trifiro[55], S. Tripathy[49], T. Tripathy[48], S. Trogolo[28], G. Trombetta[32], L. Tropp[37], V. Trubnikov[2], W.H. Trzaska[126], T.P. Trzcinski[142], B.A. Trzeciak[63], T. Tsuji[132], A. Tumkin[108], R. Turrisi[56], T.S. Tveter[20], K. Ullaland[21], E.N. Umaka[125], A. Uras[135], G.L. Usai[23], A. Utrobicic[98], M. Vala[37], N. Valle[139], S. Vallero[58], N. van der Kolk[63], L.V.R. van Doremalen[63], M. van Leeuwen[63], P. Vande Vyvre[33], D. Varga[145], Z. Varga[145], M. Varga-Kofarago[145], A. Vargas[44], M. Vasileiou[83], A. Vasiliev[87], O. Vázquez Doce[104,117], V. Vechernin[112], A.M. Veen[63], E. Vercellin[25], S. Vergara Limón[44], L. Vermunt[63], R. Vernet[7], R. Vértesi[145], L. Vickovic[34], Z. Vilakazi[131], O. Villalobos Baillie[110], A. Villatoro Tello[44], G. Vino[52], A. Vinogradov[87], T. Virgili[29], V. Vislavicius[88], A. Vodopyanov[75], B. Volkel[33], M.A. Völkl[102], K. Voloshin[91], S.A. Voloshin[143], G. Volpe[32], B. von Haller[33], I. Vorobyev[104], D. Voscek[116], J. Vrláková[37], B. Wagner[21], M. Weber[113], S.G. Weber[144], A. Wegrzynek[33], D.F. Weiser[103], S.C. Wenzel[33], J.P. Wessels[144], J. Wiechula[68], J. Wikne[20], G. Wilk[84], J. Wilkinson[10,53], G.A. Willems[33], E. Willsher[110], B. Windelband[103], M. Winn[137], W.E. Witt[130], Y. Wu[128], R. Xu[6], S. Yalcin[77], K. Yamakawa[45], S. Yang[21], S. Yano[137], Z. Yin[6], H. Yokoyama[63], I.-K. Yoo[17], J.H. Yoon[60], S. Yuan[21], A. Yuncu[103], V. Yurchenko[2], V. Zaccolo[24], A. Zaman[14], C. Zampolli[33], H.J.C. Zanoli[63], N. Zardoshti[33], A. Zarochentsev[112], P. Závada[66], N. Zaviyalov[108], H. Zbroszczyk[142], M. Zhalov[97], S. Zhang[39], X. Zhang[6], Z. Zhang[6], V. Zherebchevskii[112], D. Zhou[6], Y. Zhou[88], Z. Zhou[21], J. Zhu[6,106], Y. Zhu[6], A. Zichichi[10,26], M.B. Zimmermann[33], G. Zinovjev[2], N. Zurlo[140],

[i] *Deceased*
[ii] *Dipartimento DET del Politecnico di Torino, Turin, Italy*
[iii] *M.V. Lomonosov Moscow State University, D.V. Skobeltsyn Institute of Nuclear, Physics, Moscow, Russia*
[iv] *Department of Applied Physics, Aligarh Muslim University, Aligarh, India*
[v] *Institute of Theoretical Physics, University of Wroclaw, Poland*

[1] *A.I. Alikhanyan National Science Laboratory (Yerevan Physics Institute) Foundation, Yerevan, Armenia*
[2] *Bogolyubov Institute for Theoretical Physics, National Academy of Sciences of Ukraine, Kiev, Ukraine*
[3] *Bose Institute, Department of Physics and Centre for Astroparticle Physics and Space Science (CAPSS), Kolkata, India*
[4] *Budker Institute for Nuclear Physics, Novosibirsk, Russia*
[5] *California Polytechnic State University, San Luis Obispo, California, United States*
[6] *Central China Normal University, Wuhan, China*
[7] *Centre de Calcul de l'IN2P3, Villeurbanne, Lyon, France*
[8] *Centro de Aplicaciones Tecnológicas y Desarrollo Nuclear (CEADEN), Havana, Cuba*
[9] *Centro de Investigación y de Estudios Avanzados (CINVESTAV), Mexico City and Mérida, Mexico*
[10] *Centro Fermi — Museo Storico della Fisica e Centro Studi e Ricerche "Enrico Fermi', Rome, Italy*
[11] *Chicago State University, Chicago, Illinois, United States*
[12] *China Institute of Atomic Energy, Beijing, China*

JHEP04(2020)192

[13] *Comenius University Bratislava, Faculty of Mathematics, Physics and Informatics, Bratislava, Slovakia*
[14] *COMSATS University Islamabad, Islamabad, Pakistan*
[15] *Creighton University, Omaha, Nebraska, United States*
[16] *Department of Physics, Aligarh Muslim University, Aligarh, India*
[17] *Department of Physics, Pusan National University, Pusan, Republic of Korea*
[18] *Department of Physics, Sejong University, Seoul, Republic of Korea*
[19] *Department of Physics, University of California, Berkeley, California, United States*
[20] *Department of Physics, University of Oslo, Oslo, Norway*
[21] *Department of Physics and Technology, University of Bergen, Bergen, Norway*
[22] *Dipartimento di Fisica dell'Università 'La Sapienza' and Sezione INFN, Rome, Italy*
[23] *Dipartimento di Fisica dell'Università and Sezione INFN, Cagliari, Italy*
[24] *Dipartimento di Fisica dell'Università and Sezione INFN, Trieste, Italy*
[25] *Dipartimento di Fisica dell'Università and Sezione INFN, Turin, Italy*
[26] *Dipartimento di Fisica e Astronomia dell'Università and Sezione INFN, Bologna, Italy*
[27] *Dipartimento di Fisica e Astronomia dell'Università and Sezione INFN, Catania, Italy*
[28] *Dipartimento di Fisica e Astronomia dell'Università and Sezione INFN, Padova, Italy*
[29] *Dipartimento di Fisica 'E.R. Caianiello' dell'Università and Gruppo Collegato INFN, Salerno, Italy*
[30] *Dipartimento DISAT del Politecnico and Sezione INFN, Turin, Italy*
[31] *Dipartimento di Scienze e Innovazione Tecnologica dell'Università del Piemonte Orientale and INFN Sezione di Torino, Alessandria, Italy*
[32] *Dipartimento Interateneo di Fisica 'M. Merlin' and Sezione INFN, Bari, Italy*
[33] *European Organization for Nuclear Research (CERN), Geneva, Switzerland*
[34] *Faculty of Electrical Engineering, Mechanical Engineering and Naval Architecture, University of Split, Split, Croatia*
[35] *Faculty of Engineering and Science, Western Norway University of Applied Sciences, Bergen, Norway*
[36] *Faculty of Nuclear Sciences and Physical Engineering, Czech Technical University in Prague, Prague, Czech Republic*
[37] *Faculty of Science, P.J. Šafárik University, Košice, Slovakia*
[38] *Frankfurt Institute for Advanced Studies, Johann Wolfgang Goethe-Universität Frankfurt, Frankfurt, Germany*
[39] *Fudan University, Shanghai, China*
[40] *Gangneung-Wonju National University, Gangneung, Republic of Korea*
[41] *Gauhati University, Department of Physics, Guwahati, India*
[42] *Helmholtz-Institut für Strahlen- und Kernphysik, Rheinische Friedrich-Wilhelms-Universität Bonn, Bonn, Germany*
[43] *Helsinki Institute of Physics (HIP), Helsinki, Finland*
[44] *High Energy Physics Group, Universidad Autónoma de Puebla, Puebla, Mexico*
[45] *Hiroshima University, Hiroshima, Japan*
[46] *Hochschule Worms, Zentrum für Technologietransfer und Telekommunikation (ZTT), Worms, Germany*
[47] *Horia Hulubei National Institute of Physics and Nuclear Engineering, Bucharest, Romania*
[48] *Indian Institute of Technology Bombay (IIT), Mumbai, India*
[49] *Indian Institute of Technology Indore, Indore, India*
[50] *Indonesian Institute of Sciences, Jakarta, Indonesia*
[51] *INFN, Laboratori Nazionali di Frascati, Frascati, Italy*
[52] *INFN, Sezione di Bari, Bari, Italy*
[53] *INFN, Sezione di Bologna, Bologna, Italy*
[54] *INFN, Sezione di Cagliari, Cagliari, Italy*
[55] *INFN, Sezione di Catania, Catania, Italy*
[56] *INFN, Sezione di Padova, Padova, Italy*

JHEP04(2020)192

[57] INFN, Sezione di Roma, Rome, Italy
[58] INFN, Sezione di Torino, Turin, Italy
[59] INFN, Sezione di Trieste, Trieste, Italy
[60] Inha University, Incheon, Republic of Korea
[61] Institut de Physique Nucléaire d'Orsay (IPNO), Institut National de Physique Nucléaire et de Physique des Particules (IN2P3/CNRS), Université de Paris-Sud, Université Paris-Saclay, Orsay, France
[62] Institute for Nuclear Research, Academy of Sciences, Moscow, Russia
[63] Institute for Subatomic Physics, Utrecht University/Nikhef, Utrecht, Netherlands
[64] Institute of Experimental Physics, Slovak Academy of Sciences, Košice, Slovakia
[65] Institute of Physics, Homi Bhabha National Institute, Bhubaneswar, India
[66] Institute of Physics of the Czech Academy of Sciences, Prague, Czech Republic
[67] Institute of Space Science (ISS), Bucharest, Romania
[68] Institut für Kernphysik, Johann Wolfgang Goethe-Universität Frankfurt, Frankfurt, Germany
[69] Instituto de Ciencias Nucleares, Universidad Nacional Autónoma de México, Mexico City, Mexico
[70] Instituto de Física, Universidade Federal do Rio Grande do Sul (UFRGS), Porto Alegre, Brazil
[71] Instituto de Física, Universidad Nacional Autónoma de México, Mexico City, Mexico
[72] iThemba LABS, National Research Foundation, Somerset West, South Africa
[73] Jeonbuk National University, Jeonju, Republic of Korea
[74] Johann-Wolfgang-Goethe Universität Frankfurt Institut für Informatik, Fachbereich Informatik und Mathematik, Frankfurt, Germany
[75] Joint Institute for Nuclear Research (JINR), Dubna, Russia
[76] Korea Institute of Science and Technology Information, Daejeon, Republic of Korea
[77] KTO Karatay University, Konya, Turkey
[78] Laboratoire de Physique Subatomique et de Cosmologie, Université Grenoble-Alpes, CNRS-IN2P3, Grenoble, France
[79] Lawrence Berkeley National Laboratory, Berkeley, California, United States
[80] Lund University Department of Physics, Division of Particle Physics, Lund, Sweden
[81] Nagasaki Institute of Applied Science, Nagasaki, Japan
[82] Nara Women's University (NWU), Nara, Japan
[83] National and Kapodistrian University of Athens, School of Science, Department of Physics , Athens, Greece
[84] National Centre for Nuclear Research, Warsaw, Poland
[85] National Institute of Science Education and Research, Homi Bhabha National Institute, Jatni, India
[86] National Nuclear Research Center, Baku, Azerbaijan
[87] National Research Centre Kurchatov Institute, Moscow, Russia
[88] Niels Bohr Institute, University of Copenhagen, Copenhagen, Denmark
[89] Nikhef, National institute for subatomic physics, Amsterdam, Netherlands
[90] NRC Kurchatov Institute IHEP, Protvino, Russia
[91] NRC "Kurchatov Institute" — ITEP, Moscow, Russia
[92] NRNU Moscow Engineering Physics Institute, Moscow, Russia
[93] Nuclear Physics Group, STFC Daresbury Laboratory, Daresbury, United Kingdom
[94] Nuclear Physics Institute of the Czech Academy of Sciences, Řež u Prahy, Czech Republic
[95] Oak Ridge National Laboratory, Oak Ridge, Tennessee, United States
[96] Ohio State University, Columbus, Ohio, United States
[97] Petersburg Nuclear Physics Institute, Gatchina, Russia
[98] Physics department, Faculty of science, University of Zagreb, Zagreb, Croatia
[99] Physics Department, Panjab University, Chandigarh, India
[100] Physics Department, University of Jammu, Jammu, India
[101] Physics Department, University of Rajasthan, Jaipur, India
[102] Physikalisches Institut, Eberhard-Karls-Universität Tübingen, Tübingen, Germany
[103] Physikalisches Institut, Ruprecht-Karls-Universität Heidelberg, Heidelberg, Germany

JHEP04(2020)192

[104] Physik Department, Technische Universität München, Munich, Germany
[105] Politecnico di Bari, Bari, Italy
[106] Research Division and ExtreMe Matter Institute EMMI, GSI Helmholtzzentrum für Schwerionenforschung GmbH, Darmstadt, Germany
[107] Rudjer Bošković Institute, Zagreb, Croatia
[108] Russian Federal Nuclear Center (VNIIEF), Sarov, Russia
[109] Saha Institute of Nuclear Physics, Homi Bhabha National Institute, Kolkata, India
[110] School of Physics and Astronomy, University of Birmingham, Birmingham, United Kingdom
[111] Sección Física, Departamento de Ciencias, Pontificia Universidad Católica del Perú, Lima, Peru
[112] St. Petersburg State University, St. Petersburg, Russia
[113] Stefan Meyer Institut für Subatomare Physik (SMI), Vienna, Austria
[114] SUBATECH, IMT Atlantique, Université de Nantes, CNRS-IN2P3, Nantes, France
[115] Suranaree University of Technology, Nakhon Ratchasima, Thailand
[116] Technical University of Košice, Košice, Slovakia
[117] Technische Universität München, Excellence Cluster 'Universe', Munich, Germany
[118] The Henryk Niewodniczanski Institute of Nuclear Physics, Polish Academy of Sciences, Cracow, Poland
[119] The University of Texas at Austin, Austin, Texas, United States
[120] Universidad Autónoma de Sinaloa, Culiacán, Mexico
[121] Universidade de São Paulo (USP), São Paulo, Brazil
[122] Universidade Estadual de Campinas (UNICAMP), Campinas, Brazil
[123] Universidade Federal do ABC, Santo Andre, Brazil
[124] University of Cape Town, Cape Town, South Africa
[125] University of Houston, Houston, Texas, United States
[126] University of Jyväskylä, Jyväskylä, Finland
[127] University of Liverpool, Liverpool, United Kingdom
[128] University of Science and Techonology of China, Hefei, China
[129] University of South-Eastern Norway, Tonsberg, Norway
[130] University of Tennessee, Knoxville, Tennessee, United States
[131] University of the Witwatersrand, Johannesburg, South Africa
[132] University of Tokyo, Tokyo, Japan
[133] University of Tsukuba, Tsukuba, Japan
[134] Université Clermont Auvergne, CNRS/IN2P3, LPC, Clermont-Ferrand, France
[135] Université de Lyon, Université Lyon 1, CNRS/IN2P3, IPN-Lyon, Villeurbanne, Lyon, France
[136] Université de Strasbourg, CNRS, IPHC UMR 7178, F-67000 Strasbourg, France, Strasbourg, France
[137] Université Paris-Saclay Centre d'Etudes de Saclay (CEA), IRFU, Départment de Physique Nucléaire (DPhN), Saclay, France
[138] Università degli Studi di Foggia, Foggia, Italy
[139] Università degli Studi di Pavia, Pavia, Italy
[140] Università di Brescia, Brescia, Italy
[141] Variable Energy Cyclotron Centre, Homi Bhabha National Institute, Kolkata, India
[142] Warsaw University of Technology, Warsaw, Poland
[143] Wayne State University, Detroit, Michigan, United States
[144] Westfälische Wilhelms-Universität Münster, Institut für Kernphysik, Münster, Germany
[145] Wigner Research Centre for Physics, Budapest, Hungary
[146] Yale University, New Haven, Connecticut, United States
[147] Yonsei University, Seoul, Republic of Korea

JHEP04(2020)192